university of groningen / faculty of science and engineering

University of Groningen

Master Research Project

Development and implementation of a travelling wave ion mobility spectrometry stage

Author: M.J. Nieuwenhuis

First examiner: dr. T.A. Schlathölter
Second examiner: prof. dr. ir. C.H. van der Wal

May 4, 2021

Abstract

Mass spectrometry is a widely used technique in which ions are discriminated according to their mass-to-charge ratio, but its inability to distinguish different conformations with identical m/q presents a significant weak point. Herein the development of a travelling wave Ion Mobility Spectrometry (TW-IMS) stage to be added to an existing home-built tandem mass spectrometer system is reported. This stage uses the Structures for Lossless Ion Manipulations (SLIM) technique, where the propagation speed of ions through the device is determined by dynamic local electric fields caused by travelling voltage waves, together with collisions with He buffer gas molecules. The array of electrodes that provides the travelling wave field is patterned on printed circuit boards. The drift velocity is related to the collisional cross section and, therefore, to the molecular conformation. Depending on this relation, i.e. their mobility, ions may or may not keep up with the voltage wave. Thus, mobility separation is based on differences in arrival times at the end of the board. This technique allows the usage of long ion paths with minimum losses, resulting in good mobility resolution.

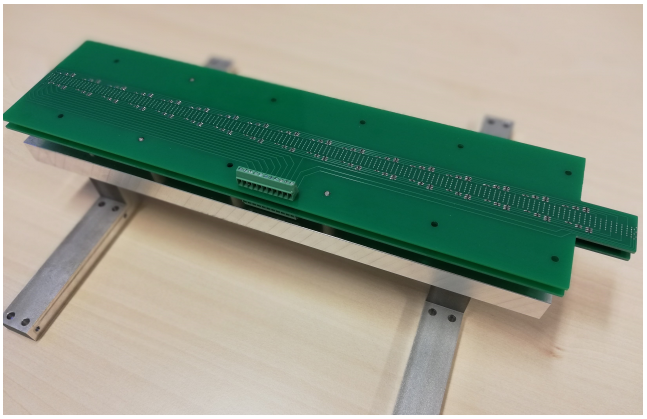

Contents

Chapter 1

Introduction

Nowadays, cancer is one of the leading causes of death. In 2020, an estimated 19.3 million new cancer cases and almost 10.0 million cancer deaths occurred worldwide [1]. Despite these terrifying numbers, survival rates have improved for many cancer types in the last half century, due to more knowledge on the causes of cancer and better treatment options. Most known and used treatments are the classical surgery, chemotherapy and radiotherapy. Especially this last technique is often involved in treatment plans for tumor control. By means of ionizing radiation, cancer cells are killed locally while the healthy tissues surrounding them are more or less spared.

The response of these cells to the action of ionizing radiation is not well understood, but seems strongly influenced by telomeres [2]. These are protective caps at the end of chromosomes and contain repeats of the specific nucleobase sequence dTTAGGG. In normal cells, they shorten with each successive cell division, but this process can be counteracted by the enzyme telomerase, that elongates the telomeres. The same enzyme is also overexpressed in 85-90 % of all cancers which protects the cancer cells from aging and dying [3]. Blocking the activity of telomerase is therefore seen as an attractive strategy in cancer therapy [4]. Structures that can do so are stabilized G-quadruplex structures, that consist of folded dTTAGGG repetitions. By investigating the interaction of ionizing radiation with oligonucleotides (the building blocks of DNA) containing the telomere sequence and with G-quadruplexes, the influence of telomerase dysfunction and telomere length on the cell's sensitivity to radiation can be explored.

This study is one of the researches conducted by the Quantum Interactions and Structural Dynamics group. Main focus of the group is to investigate the structure and structural dynamics of gas-phase biomolecules by employing atomic and molecular physics experimental techniques. These molecules can fold themselves into different structures by for instance forming intramolecular hydrogen bonds. Already many experimental techniques have been developed for investigating this folding. Since in living organisms, molecules are mostly found in the liquid environment of biological cells, these methods are employed in solutions. However, many of the most powerful approaches for molecular structure determination are gas-phase techniques, i.e. without a chemical environment [5]. Gas-phase experiments for example give the possibility to discriminate intrinsic molecular properties from effects of the chemical environment and to compare experimental data to quantum chemical calculations on a very high level of accuracy.

For these experiments, the group uses a home-built tandem mass spectrometer named "Paultje". This device brings biomolecular ions into the gas-phase, traps them and subsequently irradiates them. The products of the interaction between the ions and the radiation are then investigated, which gives insight in the structure, behaviour and dynamics of the biomolecular ions under investigation. Experiments are often performed at large scale facilities such as third generation synchrotrons or facilities for fast ion research. A few examples of experiments are soft X-ray and VUV photoabsorption studies on peptides and proteins, G-quadruplexes, polyaromatic hydrocarbons (PAH) and keV ion collision experiments [6]. In order to perform these experiments the setup of Paultje has been improved continuously since it became operational in 2009. In this project, a next improvement is described, namely the ability to control the conformational state of the biomolecular ions that are being investigated. In its current state, Paultje

can discriminate ions according to their mass-to-charge ratio, but not on conformation. For biological systems, precise structural information is of extreme importance, as the function of a biomolecule is usually defined by its conformation. The shape of an enzyme for example determines whether or not it can bind a specific molecule to provide a reaction favorable environment. Conformation is also of importance when considering interactions with radiation. An Auger electron caused by radiation for instance can cause excitation at different atoms of the molecule depending on its precise conformation. Another example is the G-quadruplex, where photoionization can lead to the formation of a valence hole that migrates towards an energetically favorable site [4]. Here it can weaken or ultimately even break bonds, which has a large impact on the structure. By comparing structures before and after irradiation, this change in structure can be investigated.

The above mentioned examples show that conformation is a key property and controlling it will be valuable in research of ion-radiation interactions. To do so, an ion mobility spectrometry (IMS) stage has been developed in the Master Research Project reported here, that will serve as an extension of Paultje.

Determining the structure of polyatomic ions in the gas-phase is a challenging problem, that in the past has been approached by indirect methods such as dissociation or reactivity studies [7]. To obtain more direct information about the conformational state of these large ions, ion mobility measurements have appeared in the picture. Over the past several decades, IMS has evolved into an inexpensive and powerful analytical technique for the detection of gas-phase samples and can be found in a large range of applications, such as air and food quality analysis, drug and explosives detection and medical diagnostics [8]. In IMS, ions are separated based on the differences in their mobilities. This mobility is a measure of how fast an ion moves through a gas under the influence of an electric field and is related to the collisional cross section of the ion and, therefore, to the molecular conformation. A larger cross section means that the ion will experience more collisions with the gas molecules and hence will move slower. Due to the introduction of ways to bring large biomolecules into the gas-phase, IMS, in combination with mass spectrometry, has become popular in recent years to study biological complex samples, such as proteins [8].

The project reported here is a continuation of the Master Research Project of Klaas Bijlsma, who started on developing the IMS stage. He was not able to finish this project, but made a good foundation to build further on. This report describes the further development of the IMS extension and starts with an overview of the existing setup of Paultje, as well as explaining the theory behind ion mobility spectrometry. In Chapter 3, the development and assembly of the stage is then discussed in detail. After assembling, some first tests have been performed to see if ions could make it through the stage and this is reported in Chapter 4. The report ends with an outlook on what still needs to be done, as well as an overall conclusion of this project.

Chapter 2

Experimental Techniques

This chapter provides all knowledge needed to understand how Paultje operates at the moment and how it can be improved by means of an extending stage. It starts by giving an overview of the existing setup in Section 2.1. Here the different elements and techniques are discussed to explain how ions can be separated based on mass and charge. In the next section then, the theory behind ion mobility spectrometry is given, to demonstrate that ions can be distinguished based on conformation as well.

2.1 Current experimental setup

Paultje is a home-built mobile tandem mass spectrometer system and is named after the German scientist Wolfgang Paul, who invented the key component in the setup, the radiofrequency (RF) ion trap. For his work on the ion trap, Paul received the Nobel Prize for Physics in 1989 [9]. In this trap, biomolecular ions are confined in a 3D volume to be irradiated by photons or ions. To assure that the radiation only interacts with the isolated ions, high vacuum conditions (10^{-7} mbar) are required. Since the molecular ions are introduced into the system at atmospheric pressure, transport of ions through a set of pumping stages is necessary to reduce the pressure stepwise to the operational high vacuum in the trap [10]. A detector behind the trap then measures the signal of ions with specific mass-to-charge ratios.

Paultje has been built during the PhD project of Sadia Bari and a first version, which is described in her PhD thesis [11], became operational in 2009. The setup has been improved during the PhD projects of Olmo Gonzaled Magana and Dmitrii Egorov, of which the details are found in their theses [10] [6]. Here a brief description of the setup is given, but a more thorough discussion can be found in their theses.

Before entering the system, the biomolecular ions are brought into gas phase by electrospray ionization (ESI), after which they are introduced into the vacuum system through a capillary. To drive the ions through the system to the Paul trap, DC potential gradients are applied. Due to DC bias voltages on the different transport sections and on diaphragms between them, ions move from the high potential ESI needle to the Paul trap, held at ground potential. After leaving the capillary, ions are guided through an RF ion funnel (IF) and octupole ion guide to the first mass spectrometer stage, a quadrupole mass filter. Ions with a specific mass-to-charge ratio are then brought into the Paul trap, where they are irradated. Lastly, products of this interaction between radiation and selected biomolecular ions are analyzed in a second mass spectrometry stage, the time-of-flight (TOF) spectrometer. Figure 2.1 shows a schematic of all the different components, that are briefly discussed in the next subsections.

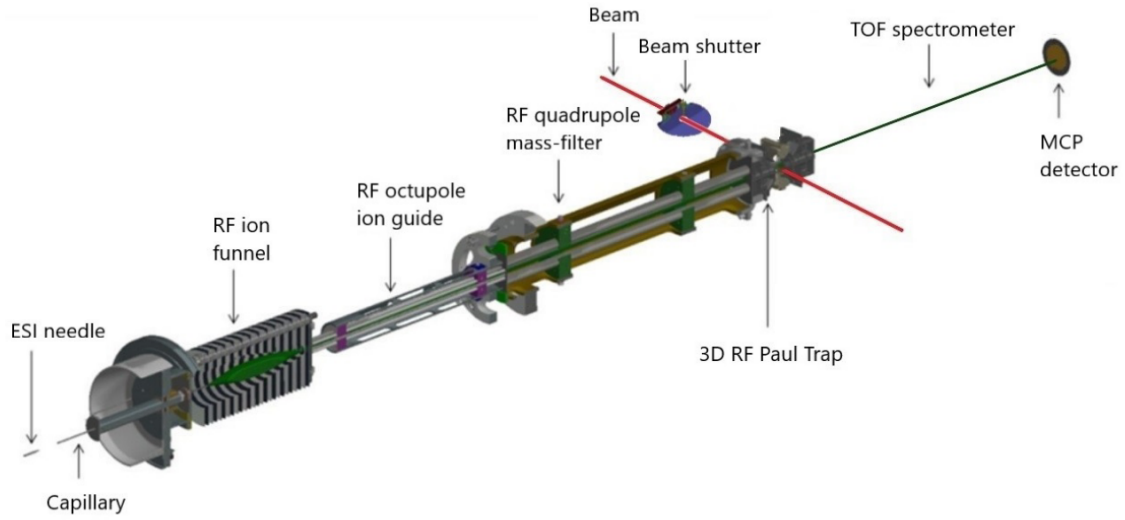

Figure 2.1: Schematic of the components of Paultje. *Image adapted from [6]*

2.1.1 Electrospray Ionization

To investigate DNA molecules via mass spectrometry, it is necessary to bring them into gas phase. However, these molecules are relatively large and therefore difficult to evaporate. Conventionally, molecules are brought into the gas phase by heating, but the large biomolecules would decompose extensively when doing so due to their weak bonds. Therefore the method of Electrospray Ionization (ESI) is used instead. A solution of molecular ions is pumped through a needle that is at a few kV relative to a capillary, through which the ions are introduced into the system. Normally this capillary is situated about 1 cm away from the needle. As more and more ions arrive at the tip of the needle, charge builds up at the surface of the pendant drop. Due to Coulomb repulsion between the charges, the fluid obtains a characteristic shape, a so-called Taylor cone. Figure 2.2 shows this formation schematically. Locally, the repulsion is larger than the surface tension holding the droplet together, and micrometer sized droplets are released as a fine spray. The droplets move towards the capillary under the influence of the electric field. Evaporation of the solvent results in a decreasing droplet diameter, while travelling towards the capillary. Due to the smaller size, the charge density on the surface increases and at some point (when the Rayleigh limit is reached), the Coulomb repulsion becomes equal to the surface tension. Result is a "Coulomb explosion" in which the droplet is torn apart and new, even smaller droplets are formed [12].

This process repeats until the droplets reach a radius of a few nanometers. Now different mechanisms can proceed, depending on the size and shape of the molecules [13]. These mechanisms are schematically shown in Figure 2.3. Low molecular weight species follow the ion evaporation model (IEM), where a small analyte is ejected from the droplet's highly charged surface by the strong electric field produced by the surface. Large globular species, such as folded proteins, follow the charged residue model (CRM), where the droplet contains one large analyte ion. Due to evaporation, the droplet shrinks. At the point all solvent molecules are evaporated, the remaining charges are taken by the analyte ion. The third mechanism, the chain ejection model (CEM), applies to unfolded proteins, where the chains are ejected stepwise. As can be seen from the figure, this mechanism has elements in common with the IEM.

The polarity of the needle can be either positive or negative, depending on if you want to obtain positive or negative ions respectively. The capillary is usually held at around 100 V of same polarity as the needle. It is heated to evaporate any remaining solvent.

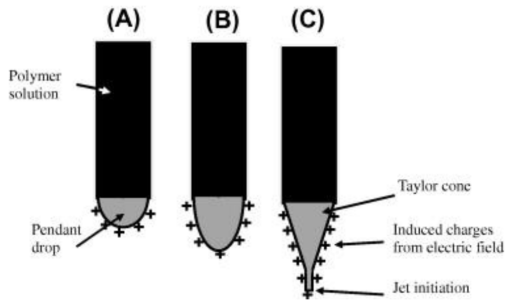

Figure 2.2: Schematic of the formation of a Taylor cone from a pendant drop. *Image from [14]*

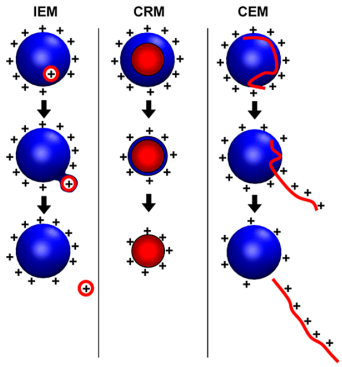

Figure 2.3: Schematic of ESI mechanisms, where blue denotes the solvent and red the analyte. *Image from [13]*

2.1.2 RF Ion Funnel

After leaving the capillary, the ion cloud expands resulting in a low ion transmission efficiency in this region [10]. In order to improve the transmission of ions and focus them to the central axis, a radiofrequency (RF) ion funnel (IF) is used to collect the expanding ions. It consists of a stack of ring-electrodes of which the internal diameter reduces along the device. Ions are focused by applying RF potentials of opposite polarity (180 degrees out-of-phase) on adjacent electrode rings, like in a stacked ring RF ion guide [16], but with the distinction that the internal ring diameter decreases. Ions are subjected to the rings' oscillating electric field, whose amplitude varies with time and axial and radial location. The time-averaged effect of a rapidly time-varying RF potential on a slow-moving ion is well represented by a static "pseudopotential" [17]. This effective potential has a distribution corresponding to a steep potential gradient near the electrodes and an almost field free region over most of the internal volume, providing a near "particle in a box" potential. This, in combination with the decreasing internal diameter, focuses the travelling ions. Following Liouvilles theorem, focusing ions in space leads to a broadening in their velocities. Liouville namely states that the density of a phase space (in which every degree of freedom or

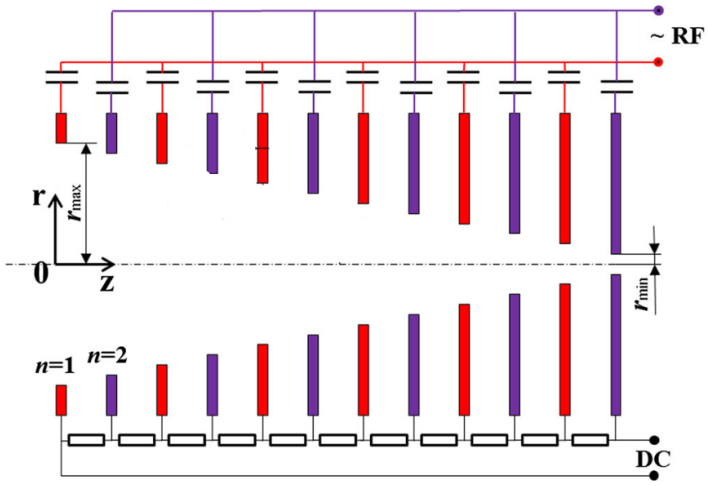

Figure 2.4: Schematic of a cross section of an RF ion funnel, where ions move from left to right while the inner diameter of the electrodes decreases. *Image adapted from [15]*

parameter of the system is represented as an axis of a multidimensional space) of any system of particles subject to conservative forces behaves like an incompressible fluid [11]. Focusing of an ion beam, i.e. an increase of position space density, is thus only possible by a decrease of the momentum space density (broader range of velocities). To prevent this, the ions must collide with other particles to remove their kinetic energy. Therefore a relatively high pressure in the $1-10^{-2}$ mbar range inside the funnel chamber is needed. To drive the ions along the axis, a DC potential gradient is applied to the ring electrodes. How the RF signal and DC potential gradient are applied to the electrodes is shown schematically in Figure 2.4.

2.1.3 RF Octupole Ion Guide and Quadrupole Mass Filter

After being focused by the ion funnel, the ions enter the first mass spectrometry stage where they are mass-selected. Here, a pressure of 10^{-6} mbar is maintained, such that an RF quadrupole mass filter can select ions with a specific m/z ratio from the pool of charge states produced by the ESI source. Thereby, ions with absorbed contamination and other unwanted species can be excluded. The device consists of four metallic rods onto which RF and DC voltages are applied. The RF signal between adjacent rods is phase shifted by 180 degrees, like in the RF ion funnel. The path of ions travelling through the device is affected by the electric fields from the rods, as shown schematically in Figure 2.5. The dynamics of a charged particle being surrounded by the 4 rods and hence experiencing a quadrupole potential can be described by Mathieu equations [10]. The stability of an ion trajectory is defined by the dimensionless, mass-dependent parameters a and q that show up in these Mathieu equations [18]. x,y-coordinate stability and instability regions can be mapped in an $a-q$ plot and one such stability region is shown in Figure 2.6. In order to guide the ions along the z-axis without hitting the rod electrodes (hence without changing their (x,y) position), a and q should be located in the overlapping stability regions of x and y. The amount of stable m/z values is reflected in the portion of a mass scan line, showing the ratio of DC over RF amplitude, that falls in this region. By scanning the amplitudes of the RF and DC voltages along the mass scan line, a mass spectrum is obtained. The closer this line is to the apex of the stability area, the smaller the part that is inside this region. This means that the range of m/z values of ions that reach the end of the quadrupole decreases, which results in a higher resolving power of the mass filter [18].

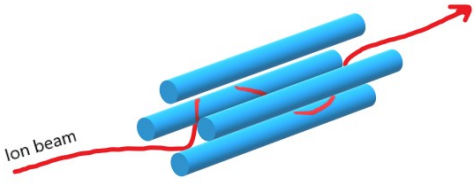

Figure 2.5: Schematic of an ion path through an quadrupole

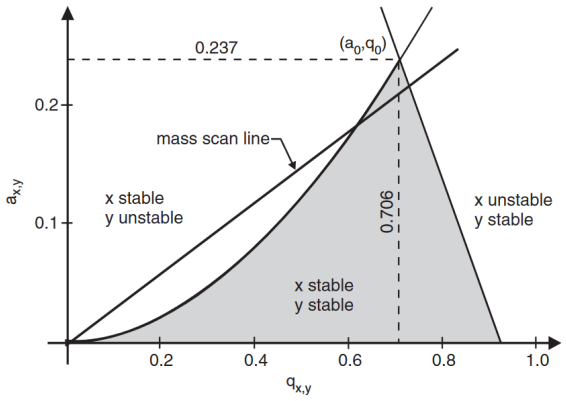

Figure 2.6: Zoomed-in a-q plot where the grey area denotes an x,y-stability region. The portion of the mass scan line that is in this grey region reflects the amount of stable m/z values. *Image from [18]*

Since pressure difference between the ion funnel and quadrupole is more than 4 orders of magnitude, this cannot be maintained via differential pumping, that works up to roughly 3 orders of magnitude. Before the ions can be mass-selected in the quadrupole, the pressure must drop, meaning that another ion guiding stage is needed. This stage is the RF octupole ion guide, that operates at a pressure of 10^{-4} mbar. It is a similar device as the quadrupole, but with 8 instead of 4 rods. In contrast to the quadrupole, it cannot filter on mass, but only guide ions through it. Looking again at Figure 2.6, for a fixed RF frequency and given mass, a solely depends on the DC voltage and q solely on the RF voltage. This means that by keeping a practically zero DC voltage ($a \approx 0$) and applying an RF potential only, there are many stable q values and hence there is a broad range of m/z valued ions that will have a stable motion and are guided through the device [18].

Behind the octupole and quadrupole biased diaphragms are placed that serve as electrostatic barriers. Above a specific voltage, ions are blocked, but below a certain value the ions can pass. By controlling this periodically, ions escape in short pulses into the next element.

2.1.4 3D RF Paul Trap

After leaving the quadrupole, the mass selected ions enter the Paul trap, by being focused by an (electrostatic) Einzel lens [6]. This trapping device, in which the ions are trapped to be exposed to radiation, has a similar working principle as the octupole and the quadrupole. An RF-voltage is applied to a central hyperbolic ring electrode, enclosed by two hyperbolic end cap electrodes as shown in Figure 2.7 [10]. The strength of the DC bias applied to the end cap electrodes then determines the m/z range for trapping, as described in the previous section. In the Paul trap, pressure is held at 10^{-7} mbar. A helium buffer gas that is pulsed in periodically facilitate dissipation of the kinetic energy of ions entering the trap through collisional cooling, such that the ions are confined in a 3D region with a size of a few hundred micrometers [19]. The trapped ions are exposed to the radiation by opening a beam shutter. To prevent the ions for being hit multiple times, the exposure time is such that about 10 percent of the ions are hit by radiation. Energetic dissociation products from the ion-radiation interaction are cooled down by applying a second buffer gas. Then by turning the RF trap off and applying a DC gradient to the two cap electrodes, the ions are removed from the trap and directed to the last element before arriving at the detector.

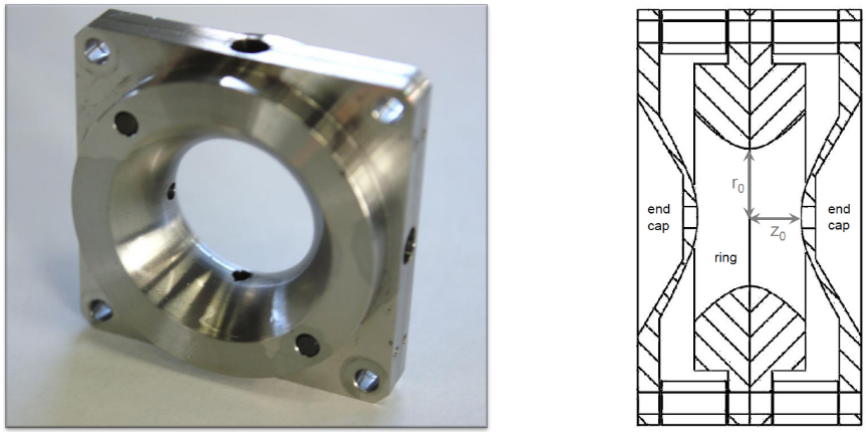

Figure 2.7: *Left:* Picture of the Paul trap ring electrode. *Right:* Schematical cross section of the Paul trap. *Image from [10]*

2.1.5 Time-of-Flight Mass Spectrometer

This last element is the time-of-flight (TOF) tube. Due to the DC voltage mentioned in the last section, particles are accelerated while moving through the tube towards the detector [20]. In this tube, in which a pressure in the range of 10^{-7} mbar is maintained, ions of the same charge acquire the same potential energy from the acceleration voltage. This energy is converted into kinetic energy and since their charges are already the same, different arrival times are based on mass. Heavier ions will be accelerated less and will have a lower velocity than lighter ones, and hence they will arrive at a later time. By measuring the arrival times a mass spectrum (intensity vs m/z) can be made. There are multiple types of TOF mass spectrometers and the one used in Paultje is the so-called reflectron. It can focus narrow packets of ions in time with a wide spread of kinetic energies excellently [21]. In the device, the particle trajectory is reversed at the end of the tube using an additional electric field. Particles entering the tube do not all have the same kinetic energy due to slight differences in position at the moment they start to accelerate. Ions that are further away from the detector are accelerated over a longer distance and hence acquire a higher kinetic energy than ones closer to, resulting in an earlier arrival at the detector. With a linear TOF spectrometer, measurements would suggest that the detected ions have different masses, which is not correct. The reflectron can compensate for these energy differences by reflecting the particles by an electric field, such that higher energy ions take a longer path, but arrive at the same time at the detector as the lower energy ones, see Figure 2.8.

The detector is situated at the beginning of the TOF tube. It consists of 3 elements, starting with a microchannel plate (MCP) that attracts the ions due to the polarity of the front side. When an ion hits the inside of one of the many channels in the MCP, an electron is kicked out and accelerated through the channel, because the backside of the MCP is biased at a higher voltage. By collisions with the channel wall, more and more electrons are generated. The electrons are attracted to the second element behind the MCP, the scintillator, that has a higher bias than the back of the MCP. Here the electrons excitate particles by collisions and in the de-excitation process photons are emitted. These photons are then detected by the third element, the photonmultiplier tube (PMT). Incoming photons hit a photocathode, which emits electrons due to the photoelectic effect. These electrons are then multiplied by the process of secondary emission. A digitizer at ground potential then detects the number of electrons (for example an oscilloscope).

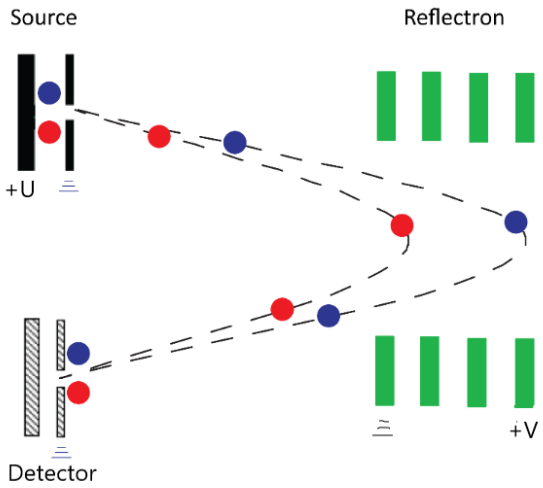

Figure 2.8: Principle of a reflectron, where negative ions of equal mass are detected. Blue has a higher energy than red and takes a longer path, but arrives at the same time at the detector as red. *Image adapted from [22]*

The mass spectrum is made based on 3 different scans to eliminate the contribution of contamination of the buffer gas or neutral molecules from the ESI source. Firstly, the TOF spectrum resulting from irradiation of trapped molecules and neutral residual gas is recorded. Secondly, the radiation source is switched off and a TOF spectrum of the initial trap content only is recorded to obtain the mass spectrum of the initial trap content. For the third scan, the ESI source is switched off and the TOF spectrum resulting from the ion–induced ionization of residual gas molecules was recorded. The latter two spectra are then subtracted from the first scan. This cycle of scans is then repeated to assure that long term fluctuations of molecule- and projectile–ion currents are averaged out.

2.2 Ion Mobility Spectrometry

With the elements discussed in the previous section, Paultje is able to trap mass-selected biomolecules. Unwanted molecules and ions are filtered out, and from the remaining desired particles, one charge state is selected and irradiated in the trap. However, these particles cannot be separated based on conformation with the device. In order to see the structural changes of molecules induced by radiation, you need to start with a well-defined conformation. It is therefore necessary that the Paul trap is loaded by molecules of a single conformation. To select these particles, the technique of ion mobility spectrometry (IMS) will be applied. In this section, this technique is explained. Firstly the concept of ion mobility is introduced, which will be used to explain ion mobility spectrometry in the next subsection. Here the discussion will be focused on a specific form of IMS, namely travelling wave IMS (TW-IMS). Lastly, the concept of structures for lossless ion manipulation (SLIM) is explained, which is framed as an extension of the TW-IMS.

2.2.1 Ion Mobility

As the name already suggests, in ion mobility spectrometry, you look at the behaviour of moving ions. Based on their mobility, different ions can be separated and identified. In IMS, gas-phase ions move under the influence of an electric field E through a buffer gas. The electric field causes the ions to accelerate, but due to collisions with the buffer gas molecules they also get decelerated. The net result is a constant drift velocity v_d. The ratio of this drift velocity and the electric field is given by the mobility K, which is a measure of how rapidly the ion moves [7]:

$$K = \frac{v_d}{E}. \tag{2.1}$$

Hence a stronger electric field results in a higher drift velocity, as the mobility of an ion stays constant. By determining the amount of time it takes for a short packet of ions to travel through a drift tube, the mobilities of the ions are measured. These mobilities are species-specific and depend amongst others on the geometry of the ions. Roughly you can say that the ion mobility is inversely proportional to the collisional cross section σ. The larger this cross section, the higher the chance for the ion to collide with a buffer gas molecule, resulting in a lower drift velocity at a specific electric field value. To find the exact relation between K and σ, kinetic gas theory is used, which is valid when the particle diameter is much smaller than its mean free path. Revercomb and Mason [23] provide a detailed derivation of the mobility following the kinetic gas theory, of which a summary is given here.

Consider collisions of moving ions of mass m and charge $q = ze$ with motionless neutral buffer gas molecules of mass M. Here, z denotes the charge state of one ion, while e is the elementary charge. Upon collision, momentum is conserved. This momentum conservation is expressed as

$$m\langle\overrightarrow{v}\rangle + M\langle\overrightarrow{V}\rangle = m\langle\overrightarrow{v}'\rangle + M\langle\overrightarrow{V}'\rangle, \tag{2.2}$$

where velocities of ions before and after the collision are denoted by the lower-case v and v' respectively and the ones of the buffer molecules by capital V and V'. The brackets indicate averages over many collisions. Now by definition, $\langle\overrightarrow{v}\rangle = v_d$, and because it is assumed that the buffer gas molecules are not moving, $\langle\overrightarrow{V}\rangle = 0$. Furthermore, when considering the centre-of-mass frame, the scattering of collided

particles is random in all directions, resulting in a zero average relative velocity after collision and hence $\langle \overrightarrow{v}' \rangle = \langle \overrightarrow{V}' \rangle$. Then Equation 2.2 becomes

$$v_d = \left(1 + \frac{M}{m}\right) \langle \overrightarrow{V}' \rangle. \tag{2.3}$$

Between collisions, the ions are accelerated by the electric field and experience a force $ma = qE$. The average velocity gained during this acceleration depends on the time between two collision, the so-called mean scattering time τ, and is expressed as $\langle \overrightarrow{v}_{gain} \rangle = a\tau$. With this velocity, the average gained momentum can be calculated as well with $m\langle \overrightarrow{v_{gain}} \rangle = qE\tau$. Upon collision, this momentum is transferred from the ions to the buffer gas molecules, resulting in movement of these molecules. Hence the molecules obtain a non-zero velocity and their average value is expressed as

$$\langle \overrightarrow{V}' \rangle = \frac{qE\tau}{M}. \tag{2.4}$$

This velocity then can be substituted in Equation 2.3 to arrive at a nice expression of the drift velocity, where the reduced mass $\mu = \frac{mM}{m+M}$ is introduced:

$$v_d = \frac{qE\tau}{\mu}. \tag{2.5}$$

The mean scattering time can be found by standard calculation of elementary kinetic theory, where ions with an average relative velocity to the motionless molecules, $\langle \overrightarrow{v}_r \rangle$, travel a distance $\langle \overrightarrow{v}_r \rangle \tau$ in time τ before they collide. This distance is called the mean free path. Assuming a hard-sphere potential, collision occurs when the surfaces of the spherical particles touch. This is the case if the distance of their centers is smaller than the sum of the radii of the two particles d [24]. Hence a moving particle can be seen as being surrounded by a theoretical circle of area σ that, when being penetrated by the center of a different stationary particle, indicates that the two particles collide. The area σ is called the collisional cross section and is given by

$$\sigma = \pi d^2. \tag{2.6}$$

In between collisions, ions move through a volume of a length equal to the mean free path and with faces equal to the collisional cross section σ. This collision cylinder is shown in Figure 2.9, where collisions occur between two equally sized particles. Exactly one particle is situated in the cylinder that has a volume of $\langle \overrightarrow{v}_r \rangle \tau\sigma$, which means that the number density N is given by $N = \frac{1}{\langle \overrightarrow{v}_r \rangle \tau\sigma}$. The expression for τ is then obtained by rearranging this formula:

$$\tau = \frac{1}{\langle \overrightarrow{v}_r \rangle N\sigma}. \tag{2.7}$$

The average relative velocity $\langle \overrightarrow{v}_r \rangle$ can be reasonably approximated by its root-mean-square value $\sqrt{\langle v_r^2 \rangle}$. Noting that now the gas molecules do have an initial velocity $\langle V \rangle$ and being in the limit of weak electric field, which means that the only contribution to the energy of the particles is thermal energy, $\langle v_r^2 \rangle$ is found via vector analysis. It can be expressed in terms of the Boltzmann constant k and temperature T, such that the formula of the average relative velocity becomes:

$$\langle \overrightarrow{v}_r \rangle \approx \sqrt{\langle v_r^2 \rangle} = \sqrt{\frac{3kT}{\mu}}. \tag{2.8}$$

This velocity can be substituted in Equation 2.7 to obtain an expression for τ, that can be subsequently entered in Equation 2.5. Then the final formula for the drift velocity has the form:

$$v_d = \frac{qE}{N\sigma} \frac{1}{\sqrt{3kT\mu}}. \tag{2.9}$$

Finally, the expression for the mobility is obtained by dividing Equation 2.9 by the electric field E

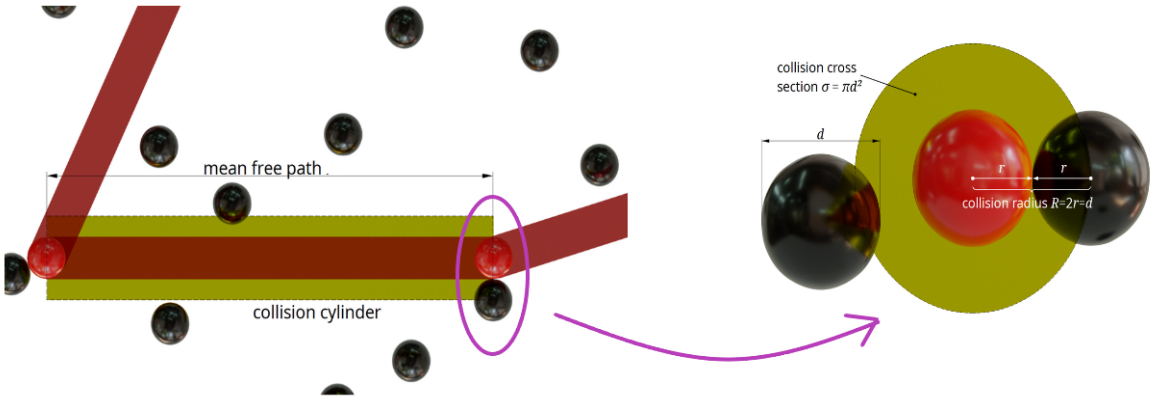

Figure 2.9: Schematic of the motion of a red particle that has collisions with black equally sized stationary particles. Dimensions of the collision cylinder are determined by the mean free path between collisions and the collisional cross section. *Image adapted from [24]*

$$K = \frac{ze}{\sqrt{3N}} \frac{1}{\sqrt{\mu kT}} \frac{1}{\sigma}, \tag{2.10}$$

where q has been replaced by ze.

2.2.2 Travelling Wave Ion Mobility Spectrometry

The theory discussed in the previous section can be applied to determine the collisional cross section of ions. The technique used for this is called ion mobility spectrometry, of which the French physicist Paul Langevin has laid the foundation [25]. With this technique, ions of the same mass but of different geometries can be separated by passing them through a gas-filled tube, called a drift-tube, under influence of a constant electric field. Due to their different mobilities, the ions exit the tube at different times. Travelling though a tube of length L will cost an ion with mobility K a time t given by [8]:

$$t = \frac{L}{v_d} = \frac{L}{KE}. \tag{2.11}$$

Hence, ions can be distinguished based on their mobility by looking at the different transit times. This separation technique is called drift-tube ion mobility spectrometry (DT-IMS) and it forms the basis of many other IMS techniques. In practice, DT-IMS has drawbacks. In order for the ions to have enough time to separate, the tube must be long, which in turn means that the voltage gradient from one end of the tube to the other must be large to obtain a good electric field along the tube. Both long drift tubes as well as the high voltages needed to acquire the large voltage drop are impracticable and therefore variations on DT-IMS have been introduced [8]. These all make use of the principle of having an electric field to separate ions in a gas-filled tube, but they differ amongst others in field strength and/or geometry.

One such improvement is the so-called travelling wave ion mobility spectrometry (TW-IMS), for which, in contrast to DT-IMS, no high voltages or lengthy tubes are needed. The main idea of this IMS technique is that the ions are not guided by a static global electric field, but rather by a dynamic local field, caused by a voltage wave that travels along the ion trajectory. This technique of using travelling waves was introduced by Giles et al. in 2004 [26], who discovered that for appropriate wave velocities, amplitudes and buffer gas pressures, ions could be separated based on their mobility. The travelling voltage wave is applied to a stacked-ring ion guide, in which ions are localized near the central axis by applying out-of-phase RF voltages to adjacent electrode rings, just as in a RF ion funnel [8]. A pulsed DC voltage is superimposed on the RF voltage to each electrode in succession to let the ions move along the tube. After a certain fixed pulse time, the voltage steps to the next electrode pair and so on, creating

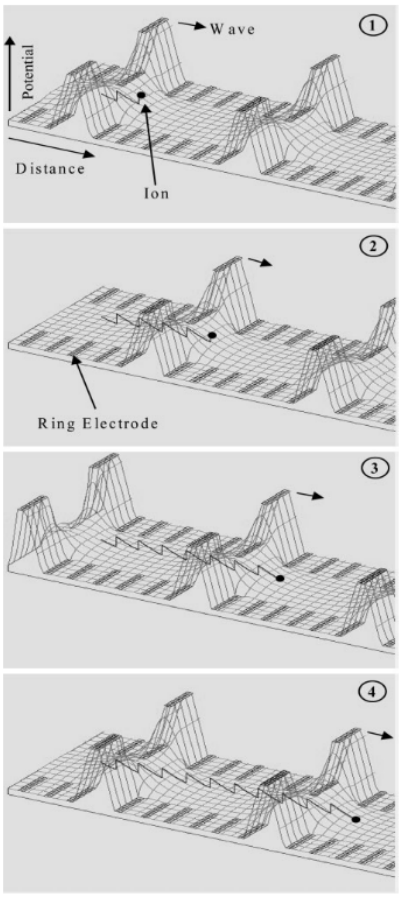

Figure 2.10: Series of SIMION plots showing a travelling potential wave that creates a moving electric field on which an ion can "surf". *Image from [26]*

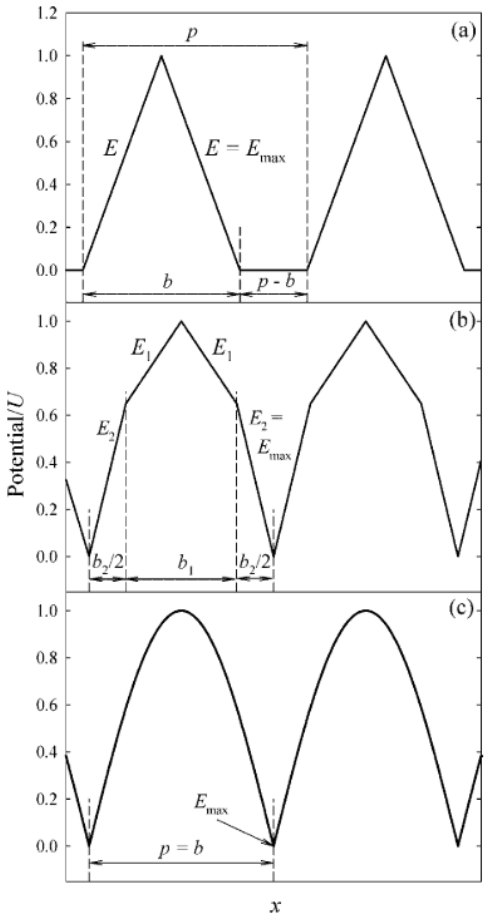

Figure 2.11: Different examples of potential wave profiles ranging from a "simple" triangular shape (a) where E-field value is constant, to a smooth profile (c) where E-field changes constantly. *Image from [27]*

a travelling voltage wave. This voltage wave generates a moving electric field that ions can feel. The electric field is like a wave on which the ion can "surf" [26]. Ions experience the field of an approaching wave and start to drift in the same direction as the wave. Figure 2.10 shows such a motion, where the ion rolls down the potential gradient away from the pulse, resulting in an axial motion along the direction of the wave to the next electrode at lower potential. Then the voltage pulse moves an electrode further, raising the potential of the electrode the ion is positioned at. As a result, the ion's potential shoots up, after which it rolls down away from the pulse again and the whole process is repeated.

Although the propagating wave pushes all ions along, their specific motion depends on the maximum ion drift velocity at the front, relative to the wave velocity [27]. As expressed in Equation 2.1, the ability of the ion to surf and keep up with the wave depends on its mobility. For drift velocities larger than the wave velocity, ions will have a net velocity equal to the wave velocity. This is because the ions will move faster than the wave, but then approach the backside of the previous instance of the wave profile. The ions are pushed back by an opposite electric field produced by the backside. Hence the ions will move at the same velocity as the wave itself and will surf nicely on it. When the ion drift velocities are much smaller, the ions cannot keep up with the wave and are passed by wave crests many times. It is

as if the wave passes underneath them [27]. The third regime, where the wave velocity is in between the maximum and minimum drift velocity values of ions from one bunch, is the most interesting one. Here the separation between higher and lower mobility ions takes place. Low mobility ions with small drift velocities are not able to keep up with the voltage wave, while higher mobility ones can. Every once in a while, the low mobility ions are passed by a wave crest, where they experience a reverse field from the backside of the crest. As a result, the ions are pushed back in space, causing a so-called roll-over event [26]. The drift velocity of the ions is, as discussed previously, determined by their cross section, hence by their mobility. The larger the cross section, the lower the mobility, and hence the lower the drift velocity, resulting in more roll-over events. The lower mobility ion therefore takes longer to traverse the tube. In this way, a bunch of ions with different mobilities can be separated based on their different arrival times.

In DT-IMS, the mobility, and hence the cross section of the ions under investigation, is obtained easily from the transit time by using Equation 2.11. This is however not the case in TW-IMS, in which an *average* ion velocity needs to be considered. When ions do not have enough speed to catch up with the wave, they are passed by the wave crest. In this process, the velocity of the ions relative to the wave velocity is changing constantly. In order to find an equation for the transit time, therefore the average velocity needs to be considered. Shvartsburg and Smith [27] developed an analytical model for that, where radially focusing RF fields are ignored, such that only the 1D transport of ions along the forward direction of the travelling wave is considered. To even further simplify the model, ion diffusion is treated independently from ion drift. To investigate this ion drift, the wave profile needs to be considered. The simplest wave profile to look at is the triangular waveform, as shown in Figure 2.11(a). With a wavelength of b and an amplitude of U, the electric field is simply given by $E = \pm 2U/b$. When an ion with mobility K and velocity $v_i = KE$ is not able to catch up with a wave of velocity v_w (meaning that $v_i < v_w$), its potential climbs the wave front with a relative velocity of $v_w - KE$. Then the wave crest is reached in a time

$$t_F = \frac{b}{2(v_w - KE)}. \tag{2.12}$$

When arrived at the crest, the electric field changes sign and the ion slides down the rear with a relative velocity $v_w + KE$. The time it takes to arrive to the baseline is then

$$t_B = \frac{b}{2(v_w + KE)}. \tag{2.13}$$

After arriving, the ion waits for the next wave for a time $t_0 = (p - b)/v_w$. One whole cycle lasts for a time $t_C = t_F + t_B + t_0$ and during this cycle the net displacement of the ion in the forward direction is equal to

$$d = v_i t_F - v_i t_B = \frac{bK^2E^2}{v_w^2 - K^2E^2}. \tag{2.14}$$

Hence the average ion velocity over the cycle is given by

$$\bar{v}_i = \frac{d}{t_C} = \frac{bv_wK^2E^2}{pv_w^2 - (p-b)K^2E^2}. \tag{2.15}$$

When ignoring ion diffusion, such that the ions are considered drift-driven only, the wave separation is set to zero. This means that $p = b$, which changes Equation 2.15 into

$$\bar{v}_i = \frac{K^2E^2}{v_w}. \tag{2.16}$$

This average velocity allows to obtain an overall transit time through a TW device of length L of

$$t_t = \frac{L}{\bar{v}_i} = \frac{Lv_w}{K^2E^2}. \tag{2.17}$$

Hence in TW-IMS, the transit time is inversely proportional to the square of the mobility, in contrast to DT-IMS (compare Equations 2.11 and 2.17).

This derivation has been done for the simple triangular wave form where the electric field has a constant value E_{max}, but can be generalized to a more realistic, smooth profile, where the electric field is changing continuously, see Figure 2.11(c). The gradual variation of the electric field intensity in the travelling wave fundamentally affects the separation properties [27]. Shvartsburg and Smith generalized that in the low mobility limit, when $K << v_w/E_{max}$, the transit time is expressed in terms of the average field intensity, $\bar{E}$, as

$$t_t = \frac{Lv_w}{K^2\bar{E}^2}. \tag{2.18}$$

For high-mobility ions, only the maximum electric field matters. This is because they are able to surf on the wave due to their high velocities. In that case, the transit time is obtained by replacing $\bar{E}$ by E_{max} in Equation 2.18.

Since in TW-IMS the transit time depends on the average ion velocity, it is not straightforward to obtain the mobility and cross section from it. In order for the transit times to be useful, the system needs to be calibrated with ions of known potential [19].

2.2.3 Structures for Lossless Ion Manipulation

Ion mobility spectrometry (and other seperation and ion manipulation techniques) coupled to mass spectrometry enables analysis of highly complex chemical and biochemical samples, but throughput and/or sensitivity often decrease when making such combinations due to for example differences in sample flow rate, carrier media and/or gas pressure conditions [28]. To enable a complex sequences of ion manipulations in one platform in which ions can be transmitted and stored with negligible losses, the concept of structures for lossless ion manipulation (SLIM) has been introduced by Richard D. Smith et al. (Pacific Northwest National Laboratory, PNNL) [29] in 2014. In the first experimental design of SLIM, two planar and parallel boards were used, that each consisted of an array of rung electrodes, bordered by DC "guard" electrodes [28]. A schematic of a segment of this design is shown in Figure 2.12. Onto the rung electrodes, both RF and DC voltages are applied, to confine ions in between the surfaces (y-axis) and to create a voltage gradient driving the ions along the rung array (z-direction) respectively. This

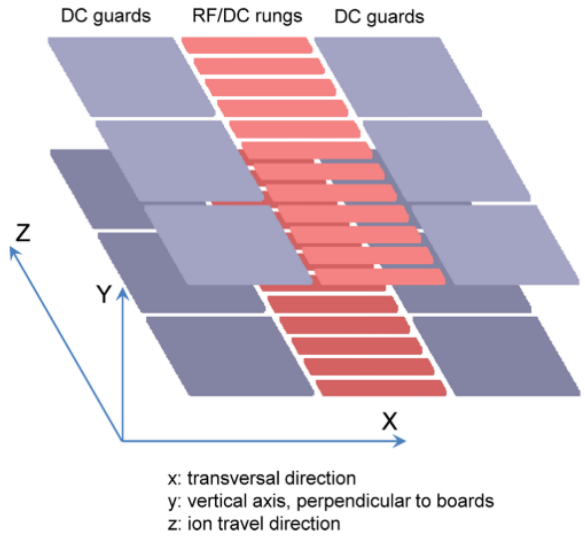

Figure 2.12: Schematic of a segment of the initial SLIM design that consists of 2 parallel planes that contain RF and DC electrodes. *Image from [28]*

working principle is similar to the one of the ion funnel and multipole devices as discussed in Section 2.1. The guard electrodes make sure that the ions are confined in the transversal direction (x-axis). Using printed circuit board (PCB) based SLIM allows for many different electrode designs to be rapidly fabricated, tested, and applied at low cost [28][30].

The SLIM module discussed so far uses constant potential fields and can be implemented in drift tube IMS. However, then there are still the high voltage requirements that limit the drift path lengths that are practical [31]. Smaller path lengths limit the achievable IMS resolution and must be avoided. Therefore a new SLIM design has been introduced in which the technique of SLIM is combined with the low voltage advantage of travelling wave IMS earlier explained. This design is referred to as travelling wave structures for lossless ion manipulation (TW-SLIM) and a segment of the PCB design is shown schematically at the top of Figure 2.13. In contrast to the constant field SLIM design that had the RF and DC potentials both applied to each rung electrode, in the TW-SLIM separate electrodes are used. Figure 2.13 shows that RF signals are applied to 6 continuous strips, with in between these strips arrays of small TW electrodes to which the DC signal is applied. Eight TW electrodes next to each other form 1 set and each electrode can be on (1, specific DC voltage is applied) or off (0, no voltage, ground potential). The bottom of Figure 2.13 shows a black-lined block wave where the first 4 electrodes are on and the last 4 are off (11110000). Then at a next time step, indicated by the red dashed line, electrode 1 is turned off, but electrode 5 is turned on (01111000). As a result, the block wave profile moves 1 electrode further. This process is then repeated for electrodes 2 and 6, 3 and 7 etc., such that the block is constantly moving.

In order to realise very long ion trajectories in a much more compact way as compared to a linear path, a serpentine-shaped path as shown in Figure 2.14 can be used. This is realised by designing a TW-SLIM module that consists of 90° turns. The electrode configuration to obtain these turns can be easily produced on PCBs. When these PCBs have the same size as the initial linear TW-SLIM system, they

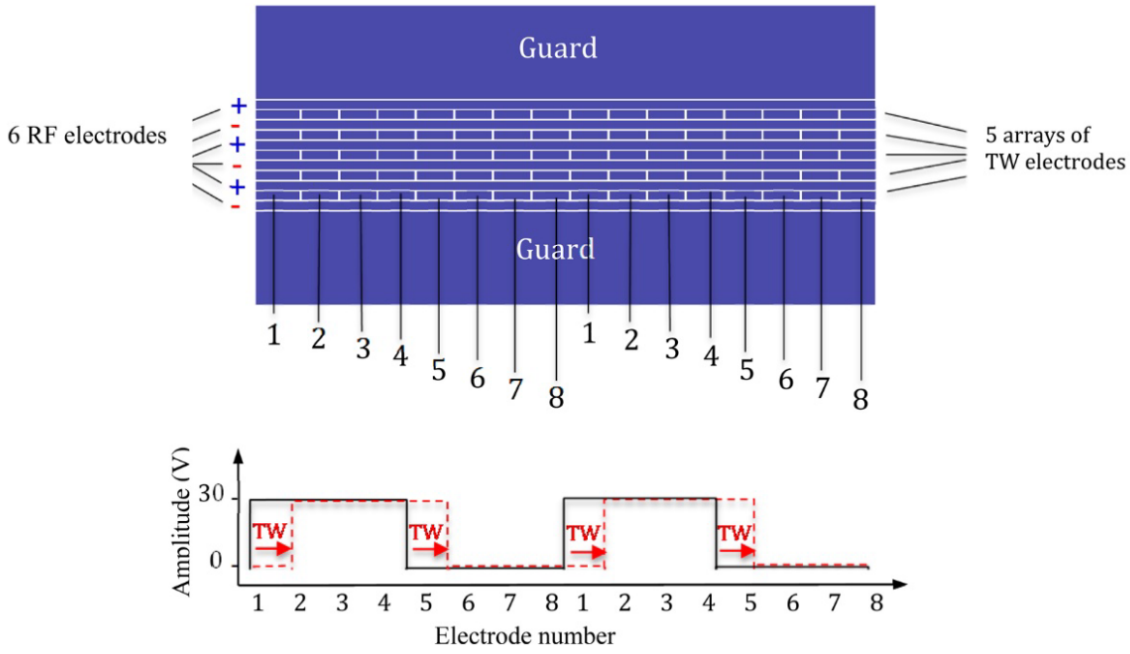

Figure 2.13: Schematics of a segment of a TW SLIM PCB design showing two sets of 8 TW electrodes (top) and of the DC voltage applied to each electrode where the red dashed line indicates the voltage profile one time step after the black line. *Image adapted from [31]*

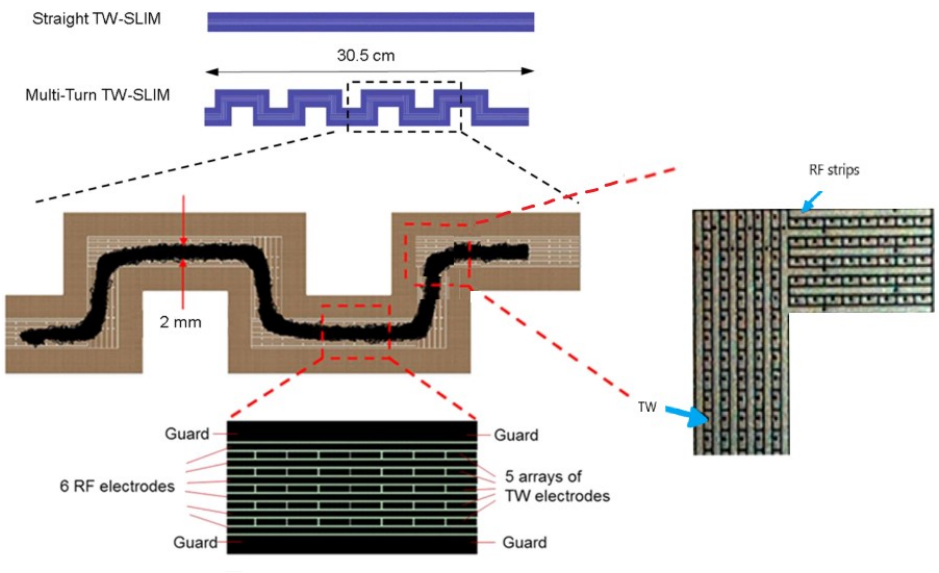

Figure 2.14: Schematics of a linear and multi-turn TW SLIM (top) together with a SIMION simulation of the trajectory of 1000 ions on a portion of the multiturn path (middle). The bottom inset shows a zoomed-in view of the electrode geometry, similar to the one in Figure 2.13, while in the right inset the electrode structure at a turn can be seen. *Image adapted from [32] and [33]*

can simply be implemented in the existing setup. This saves a lot of time and costs and therefore shows exactly one of the main advantages of SLIM. Figure 2.14 shows a SIMION simulation of the trajectory of 1000 ions on a segment of the serpentine path and as one can see, the ions are able to make the 90° turns and keep confined to the path. These ions mostly move within "travelling traps" or "bins", since the region between consecutive travelling waves acts as a small trap [34]. The ions incidentally can roll back to a previous bin based on their mobility When they arrive at a turn, the ions of an incoming bin can be effectively taken over by a bin that moves in the orthogonal direction (if the timing is right) [32]. Figure 2.15 schematically displays the potential landscape near a turn, clearly showing the traps. The plume width of the ion bunch (2 mm in Figure 2.14) is influenced by the guard electrode potential as well as the gap between the SLIM surfaces. When this plume width is smaller than the travelling bin size, complete transfer of ion plume from one bin into the orthogonal bin is possible. At a turn, it is more

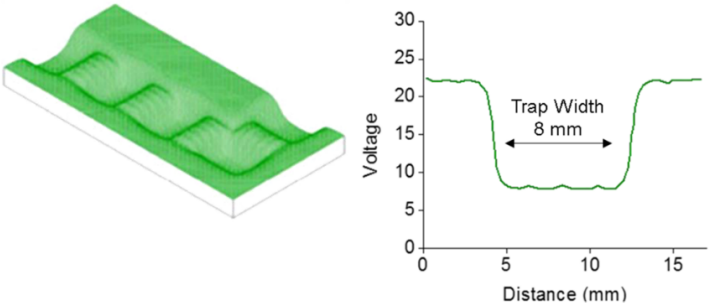

Figure 2.15: Potential energy surface from SIMION near a turn at one instant in time (left) and the voltage values along the axis of ion motion (right). *Image from [32]*

difficult to separate the ions based on mobilities, since they cannot fall back to a previous bin as soon as they are situated in the orthogonal path. This is because the turn region is confined by the guard electrodes. These inactive corners must be taken into account when considering the resolution. It turns out that there is no loss of resolution at the turns, but the turns also contribute less to increasing the resolution. In order to effectively increase the resolution, longer straight sections between turns should be taken [32].

One thing that can really increase the path length of the ions, without making the device larger is by implementing a switch. The switch, located at the end of the path, allows the user to let the ions leave the SLIM to be guided to the next element, or to be guided back to the start of the path to let the ions walk through the device another time. By applying a repulsive DC voltage to the five electrodes, that are separated from each other by the RF electrodes, in one of the two arrays, ions are directed into the other array [35]. A switch can also be used to select a portion of ions based on their conformation. By appropriate timing of the switch voltage, only a specific portion of the ions can be allowed to pass while the others are deflected. This timing depends on the transit time of the ions.

By combining the serpentine path and the switch, Deng et al. [35] were able to cycle ions through a 13.5-m serpentine ion path multiple times, achieving path lengths of kilometers and resolving powers of up to around 1860. This is far in the ultrahigh resolution regime, which we speak of when the resolving power R_p is more then 200 [36]. This resolving power is measured as the ratio of the transit time of the peak centre t_t to the full width at half-maximum of the peak Δt [32]:

$$R_p = \frac{t_t}{\Delta t}. \tag{2.19}$$

However, as the number of cycles increases, the mobility ranges become constrained. This is because the higher mobility ions will overtake the lower mobility ions that have experienced fewer passes, resulting in convolution of their arrival time distribution at the detector [36]. To obtain ultrahigh resolution over broader mobility ranges, a multilevel SLIM module has been developed very recently that contains multiple stacked serpentine paths. By means of an TW-based ion escalator, ions can be guided to a next level. In this way again a long ion path is created that increases the resolution, without using multiple passes. With this technique resolving powers up to 560 have been achieved, albeit that losses were observed for ions with low mobilities [36], demonstrating that there is enough room for improvement. The multilayer idea however is very promising, since for example also different ion chemistry on different levels could be performed [37].

Chapter 3

Development and Assembly of the TW-IMS Stage

The previous chapter explained how the current spectrometer system can be extended by means of an ion mobility spectrometry stage. In this chapter, the development and assembly of this new stage is discussed. The design concept of this extension was the topic of Klaas' Master Research Project and for the details of this design his thesis [19] can be consulted. In the previous chapter, the concept of TW-SLIM was discussed, that allows for a compact design, low voltage conditions and easy and low-cost fabrication. Because of these advantages, the new system's design has been based on this concept. The TW-SLIM stage is implemented between the ESI needle and the octupole ion guide in the current setup of Paultje and substitutes the existing ion funnel. In this chapter, first the outline of the SLIM stage is shortly discussed, after which the design of the different elements are treated individually.

3.1 Outline of Design

To be able to implement the TW-SLIM concept into practice, there is more involved than placing 2 parallel PCBs in a vacuum chamber. The ions need to be brought in between the plates in a pulsed manner and the pressure must be such that the stage can be connected to Paultje without any problem. This stage replaces the RF ion funnel in the current set up, meaning that it will be placed in between the ESI needle and the octupole. After having studied numerous articles from the PNNL group, Klaas had decided to design a specific setup [19]. A short outline of this system is given here.

The TW-SLIM is realized in the so-called "main chamber". Before ions enter this chamber, they travel through two smaller chambers that each contain an ion funnel. To compensate for the loss of ions due to selecting a conformation, a capillary with a large internal diameter is desired such that more ions can be introduced in the system in the first place. An ion funnel that works at relatively high pressure and voltage enables this increased ion inlet. Such an ion funnel is called high pressure ion funnel (HPIF). Behind the HPIF (and in front of the TW-SLIM), an ion funnel trap (IFT) is placed in a separate chamber. It guides ions like in an ordinary ion funnel, but is able to trap them as well. Then the ions can be released to the TW-SLIM periodically. The HPIF and IFT are offset from each other and from the capillary to prevent unwanted neutral molecules, that are not affected by the electric field in the funnels and hence move straight through, to enter the TW-SLIM module. After the module, a third ion funnel is placed, the so-called rear ion funnel (RIF), to focus the mobility-separated ions. The RIF operates at the same pressure as the TW-SLIM module. To be able to connect this system to the existing setup, the pressure must be reduced. A quadrupole ion guide will take on this task and guide the ions through a chamber with a pressure such that there is a nice pressure gradient from RIF to the octupole in the existing setup.

Hence to summarize, to system is built as follows: capillary - HPIF - IFT - TW-SLIM - RIF - quadrupole, see Figure 3.1. In the next sections, the individual elements are discussed in more detail.

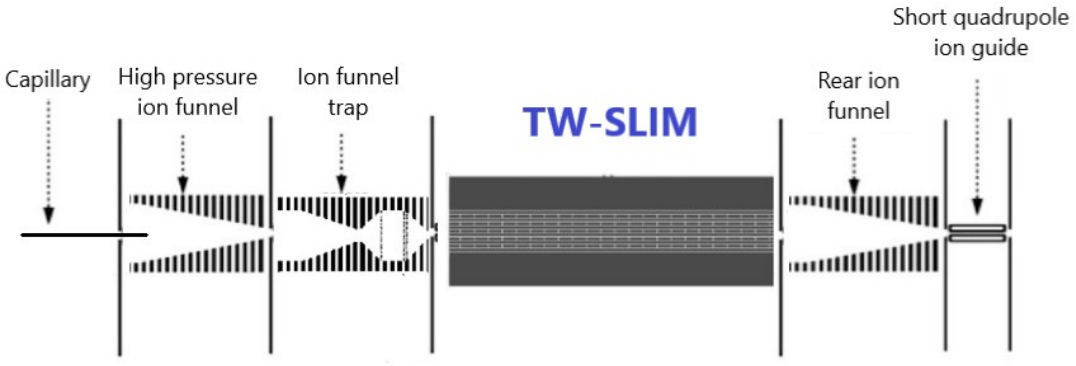

Figure 3.1: Schematic of the extending TW-IMS stage.

3.2 Vacuum Chambers

Before the different components in the system are explained, it is good to say something about the chambers in which these elements are situated. At the start of this project, these chambers, except for the quadrupole, had already been fabricated by the workshop. Here, some general information is given, mainly about the dimensions of the chambers.

It was found most suitable to make the ion funnel chambers and main chamber out of a solid piece of aluminium alloy 51ST (AlMgSi) [19]. Stress analysis by the Finite Element Method (FEM) had been performed to investigate the effect of the walls being pushed inwards due to pressure from the outside. In this way, the thickness of the walls and top and bottom plate of the main chamber was determined. It was concluded that a wall thickness of 22 mm suffices, as well as a 20 mm and 15 mm thick bottom and top plate. The length (in the direction of the ion trajectory) and width of the main chamber had been set to 335 mm and 344 mm respectively, resulting in an inner width of 300 mm which was chosen arbitrary. The height of the walls was set to 130 mm, to match with the height of the funnel chambers. Ions enter the chamber through a 25.4 mm (1 inch) diameter drilled opening, while the back side of the chamber was given an opening with a diameter of 90 mm to allow the RIF to stick out.

The HPIF and IFT are united in one so-called front chamber, which was drilled out of the remaining block of aluminium from the main chamber. This chamber consists of two compartments, each giving room to an ion funnel. These sections are cylindrically shaped with a diameter of 90 mm and are separated by a 6 mm thick wall. This wall has an opening of diameter 25.4 mm to let ions move from the HPIF to the IFT. The length of the HPIF chamber is 135 mm, while the IFT chamber has a length of 107 mm. Total length of the front chamber is therefore 248 mm. It has an outside width and height of 120 mm and 140 mm respectively. The chamber is open both at the front and back to be able to access the ion funnels. A front plate holding the capillary closes the system at one side, while the other side is connected to the side wall of the main chamber.

To the other side of the main chamber, a rear chamber is attached that holds the RIF. As in the front chamber, a cylinder of diameter 90 mm is drilled to facilitate space for the funnel. The RIF sticks out of the chamber, such that it extends into the wall of main chamber. Total outside length, width and height of this chamber are 103 mm, 130 mm and 130 mm respectively. The front is open, while in the back a 25.4 mm opening is situated. The back surface has a thickness of 20 mm and has a 5 mm deep circle milled on it. The quadrupole support disk fits neatly into here, ensuring its alignment. More about this is discussed in the section about the quadrupole.

In all but the RIF vacuum chambers, openings that are compatible with the KF-40 standard were placed on the side walls to deliver the required electrical wires, as well as ones for ISO-63 in the bottom,

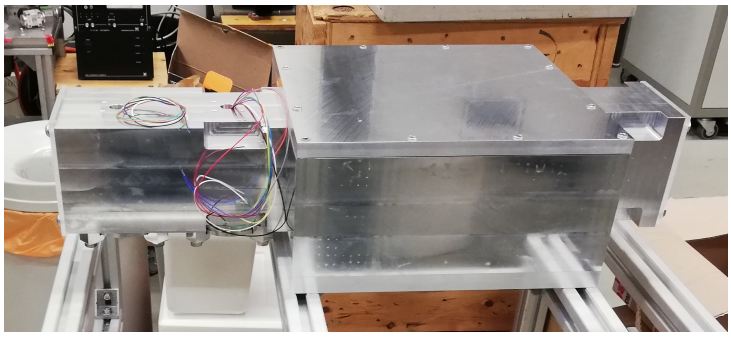

Figure 3.2: Picture of the three vacuum chambers assembled into one stage. From left to right: front chamber, main chamber, rear chamber.

to be able to connect a vacuum pump. Thereby, KF-16 openings were drilled for connecting pressure gauges on top, to monitor the pressure inside the chambers. Finally, in the main chamber an additional opening for a KF-10 flange was placed intended for a buffer gas inlet.

Figure 3.8 shows a picture of the three chambers connected to each other. Ions enter the system from the left and go subsequently through the front, main and rear chamber. The openings on the side walls and bottoms are not shown here.

Since Klaas extensively discussed the whole design process of the vacuum chambers, the information above will be all that is given about the chambers' design in this report. For an elaborate discussion and technical details, please have a look at his thesis.

3.3 ESI and Capillary

The biomolecular ions are brought into the system in the same way as in Paultje, hence by means of ESI and a capillary. The theory behind this has been discussed in Section 2.1.1. The current situation in Paultje is not ideal however. The capillary setup has been changed numerous times, which has led to an improvised arrangement that is not that practical in use. Therefore it was decided to let a mechanical

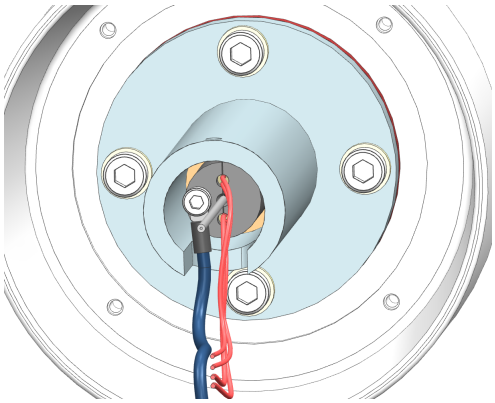

Figure 3.3: Schematic of front view of the capillary setup with the front disc removed. A wire to apply a bias and heating rods can be attached to the tube that holds the capillary.

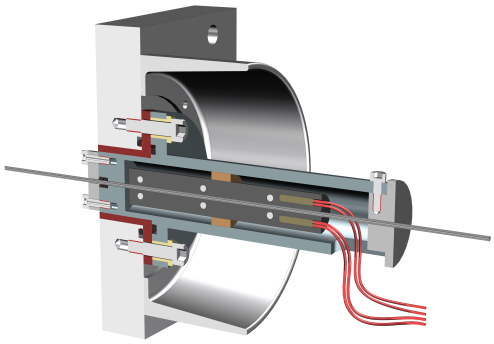

Figure 3.4: Cross section of the design of the system holding the capillary. Two heating rods (the brown tubes with the red wires) can be attached, as well as a wire to apply a potential (not showing).

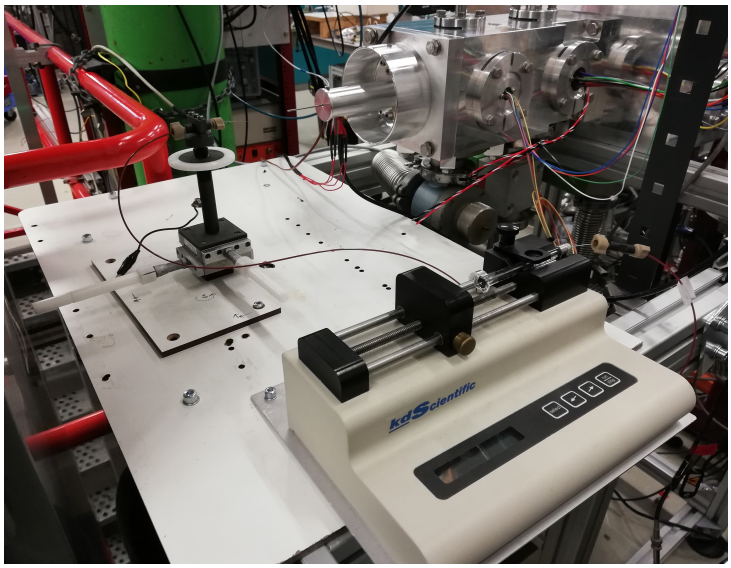

Figure 3.5: Picture of the ESI and capillary setup in front of the system.

engineer make a new design of it for the new stage [38]. Figures 3.3 and 3.4 show a schematic front view and a cross section of the design, that takes into account that the whole system must be vacuum tight and easily be taken apart. The capillary is supported by a metallic tube, into which two cylindrical holes are milled to insert heating rods. These rods heat the capillary to evaporate any remaining solvent. The supporting tube is electrically insulated and allows for application of a bias voltage through a wire. The capillary used for this project has an internal diameter of 0.5 mm, but can be replaced by a larger one in the future, such that more ions can be introduced into the system. A small front disc is placed to create a better electric field. A large cap around the tube collects all ions that do not make it into the capillary. This whole system is attached to an aluminium plate that is connected to the front of the HPIF chamber by means of screws. The capillary sticks out at the chamber side such that when ions leave the capillary, they end up in the HPIF.

Figure 3.5 shows a picture of the ESI and capillary setup installed in front of the system. The ESI needle is placed on a plateau that can be moved in the x-,y- and z-direction precisely and independently to achieve the best alignment with the capillary. A computer controlled syringe pumps the biomolecular ions through a thin hollow wire to the needle. Due to the ESI mechanism, the ions are released from the needle in small droplets and eventually reach the capillary and are introduced in the system.

3.4 Ion Funnels

To guide the ions to the SLIM module and the detector, three ion funnels are used. These funnels work according to the same principles and hence have much in common. In this section, these general characteristics are discussed, as well as how the required signals can arrive to the ion funnels. However, the funnels also have distinct unique features and therefore the separate ion funnels are briefly discussed in subsections as well.

3.4.1 Ion Funnel Characteristics

The three ion funnels (HPIF, IFT and RIF) were purchased from the company GAA Custom Engineering, LLC (Benton City, WA, USA). This company also provided the ion funnel that is already used in Paultje. The funnels work as explained in Section 2.1.2. These particular funnels consist of 100 squared insulating PCB plates, each with a conducting ring surrounding a hole. The rings have different diameters, giving

Figure 3.6: Ion funnel with two side plates, rods and the insulating spacer plates removed.

Figure 3.7: Zoom-in of the front of the ion funnel.

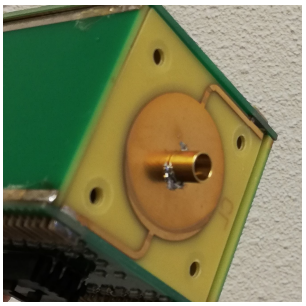

Figure 3.8: Zoom-in of the back of the ion funnel with a brass tube soldered to the CL plate.

the system its funnel-appearance to focus the ions. The plates are soldered onto two PCBs that contain the required resistors and capacitors to generate the DC and RF signals. On these boards, the connectors for the RF and DC signals are provided. Between each plate, a spacer plate is installed that has an opening, but no metal ring. These spacer plates assure electrical insulation. Figure 3.6 shows a standing cleaned ion funnel of which all spacer plates have been removed. To do so, two long outer side plates had to be removed, as well as the four PEEK rods with a length of 104.1 mm (4.1 inch) each, that keep the spacers in place. The rods can be threaded onto 4-40 set screws to mount the ion funnel to a surface. In the figure, the last plate of the ion funnel can be seen. This is the conductance limiting (CL) plate, onto which a separate potential can be applied, such that a uniform field is created behind the funnel [19]. In Figure 3.7 a zoomed-in picture of the other side of the ion funnel can be seen, which shows the inside of the ion funnel. The metal rings decrease in internal diameter, starting from 25.4 mm (1 inch), such that at the end of the funnel, only a hole of diameter 2 mm is left over for the ions to travel through.

3.4.2 HPIF

As already briefly mentioned, the first ion funnel, the HPIF, operates at relatively high pressure and voltage to enable an increased inlet of ions through the capillary. It is placed in its own chamber, in which a typical pressure of 10-15 mbar is maintained. In this way, more ions will be focused and this increases the signal obtained at the detector as compared to when only the IFT is used. Two connectors are mounted on the side boards of the funnel to connect the necessary DC and RF wires (3 and 2 respectively). The HPIF is offset from the capillary by 6 mm, such that unwanted neutral molecules are not injected on the central axis of the second funnel. These molecules are not affected by the electric field induced by the electrodes in the ion funnel and travel in a straight line through the device. Due to the offset, they simply do not pass the ion funnel but crash into its walls.

The aluminium wall that separates the HPIF and IFT chambers is 6 mm thick. This means that ions have to travel quite a distance in between the funnels with a surrounding wall at ground potential. This is a likely source of high ion losses and therefore a brass thin-walled tube is soldered onto the CL plate of the HPIF. Figure 3.8 shows this tube soldered to the CL plate. The tube has the same potential as the CL plate and guides the ions towards the entrance of the IFT.

3.4.3 IFT

After the HPIF, the second ion funnel, the IFT, is installed with an offset of 6 mm relative to the previous element. This funnel is special, since it does not only guide the ions, but also traps them. The first part of the device is similar to the HPIF described above, albeit that the internal diameter of the ring electrodes decreases faster than in the IFT. This is schematically shown as regions 1 and 2 in Figure 3.9. In section 3, the diameter increases again, to couple section 2 to the trap situated in region 4. The trap consists of 10 ring electrodes and is accumulating ions when being in trapping mode. To control the ion

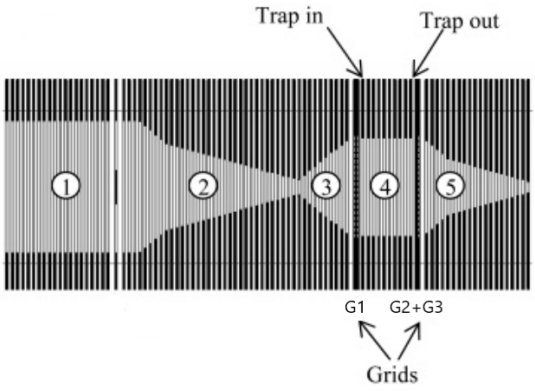

Figure 3.9: Schematic of an ion funnel trap, where the numbers refer to the different sections of the funnel. *Image adapted from [39]*

populations, storage and extraction times, pulsing voltages are applied to the three grids (G1, G2 and G3) [39]. Grid 1 is for entrance, Grid 2 and 3 for the exit (in and out respectively). By adjusting the potentials at the first and last electrodes in region 4, denoted by "Trap in" and "Trap out" in Figure 3.9, the DC gradient in the trap can be changed independently from the rest of the ion funnel. Lastly, the bunch of ions released from the trap, is focused in region 5 by means of a decreasing internal diameter of the metal rings. The RF and DC signals are provided via three connectors (for the RF, Grids and DC connections) that are mounted to the side boards of the ion funnel. The RF connector contains 2 wires, while the Grid and DC ones have 3 and 5 wires attached to them respectively.

In contrast to the HPIF, the IFT is not mounted on the wall of the front chamber, but directly on the outside wall of the main chamber. Hence when removing the front chamber from the main chamber, one must be careful to not damage the IFT.

3.4.4 RIF

The last ion funnel is placed after the TW-SLIM module in the rear chamber. The funnel is the same type as the HPIF and its chamber is open to the main chamber. The RIF sticks out of the rear chamber by 22 mm, such that it extends into the wall of the main chamber. Its front surface sits flush with the wall to let the unguided ion path between PCB and RIF be as short as possible, to prevent ion losses. The wires providing the required RF and DC signals for the funnel are delivered by a flange attached to the wall of the main chamber. These are connected to the funnel the same way as to the HPIF, so by means of two connectors, that contain 2 RF wires and 3 DC wires respectively.

3.4.5 Connectors

All connectors for the ion funnels have been provided by GAA Custom Engineering. With these connectors, to which short coloured wires are attached, wires can easily be connected to and removed from the ion funnels. The RF and DC signals are brought into the vacuum chamber by wires that go through so-called multipin feedthroughs. These are discussed in detail in Section 3.7. The wires through the feedthroughs were connected to the wires attached to the ion funnels by soldering them together. The place that was soldered, was covered by a transparant heat shrink tubing made of PTFE (Polytetrafluoroethylene) for isolation purposes. Reason to use this material is that PTFE is suitable for vacuum applications and is relatively cheap. It is even found acceptable for space use, amongst other things due to low outgassing [40]. A picture of the wiring situation from feedthrough to connector is shown in Figure 3.10. This specific picture shows the three connectors to the IFT.

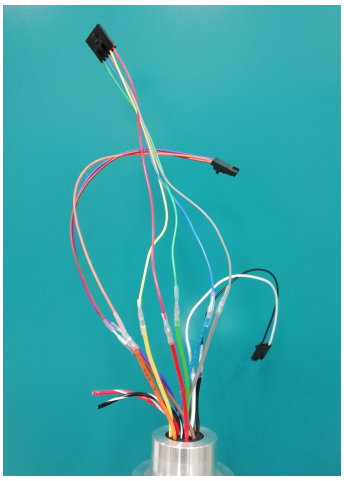

Figure 3.10: Ion funnel connectors (black) with wires that are soldered to wires from the multipin feedthrough. The solder spots have been covered by transparent heat shrink tubes.

3.5 Main Chamber

The main chamber is where the magic happens. Here the SLIM module is installed to separate the ion beam based on the mobility of the ions. This chamber is large, such that in the future large SLIM boards can be implemented that increase the separation ability and resolution. The big show pieces in this chamber are of course the two PCBs with the SLIM electrode pattern between which the ions move. Another important component is the holder onto which the PCBs are mounted. In this section, the PCB design and supporting frame are discussed in different subsections. There will also be elaborated on the way the PCBs are separated from each other.

3.5.1 PCB Design Considerations

Since the research group has no experience in using TW-SLIM, it was decided to start with a relatively simple PCB design. In this way, potential problems can be taken care of before implementation of the final complex electrode pattern. This first design is discussed extensively in this section. Due to the limited time, it was not possible in this project to design and test the final design (serpentine path, ion switch, multiple levels etc.).

The dimensions of the PCBs were partly predetermined by the size of the main chamber. When the design of this chamber was made, a conceptual PCB was designed based on the linear TW-SLIM module developed and described by Hamid et al. [31] of the PNNL group. In their study, Hamid et al. used an electrode structure as shown in Figure 2.13, where a set of eight TW electrodes, with a length and width of 1.98 mm and 0.43 mm respectively, was repeated 18 times. RF electrodes shared this same width, while the guard electrodes are 5.08 mm wide. Spacing between the electrodes was 0.13 mm. With these dimensions in mind, the length (in the direction of ion travel) and width of the main chamber were decided [19]. It is best to make a PCB design as similar as the one of Hamid et al. as possible, hence with the same amount of electrodes with the same dimensions. Especially the same spacing and width of the RF and TW electrodes are desired, since the same values have also been used in other studies [32] [33] [35] [41]. However, our PCBs were intended to be manufactured by the company Eurocircuits (Mechelen, Belgium), which PCB proto service limits the electrode spacing to a minimum value of 0.15 mm [42]. Hence the exact same dimensions as in the study of Hamid et al. could not be used. After consultation of GAA Custom Engineering, it was decided that a spacing of 0.15 mm also suffices. Moreover, by increasing the spacing the capacitance will slightly decrease, which makes it easier to drive electrode signals [43].

Besides spacing, the width and length of the electrodes were adjusted as well. In order to keep the

ratio of the dimensions in the transversal direction the same, the width was scaled by a factor of 15/13 leading to a value of 0.50 mm. In a different study of Hamid et al. [44], SIMION simulations show that similar ion confinement could be created when the electrode width increases, as long as the size of the gap between the two boards and the RF amplitude increase. Therefore it was expected that this change in width will not cause any problem, as long as the inter-surface gap and RF amplitude are adjusted correctly. In the same paper, the resolution of TW electrodes of different lengths was investigated. It was observed that for a fixed gap between the PCBs, similar resolution was attained for 1 and 2 mm long electrodes, while 4 mm electrodes had a significantly smaller optimal resolution. However, by increasing the gap, also for these longer electrodes a similar resolution was attained [44]. The study showed that comparable optimal resolution was reached at a twice as high TW speed for 1 mm electrodes (200 m/s) compared to the 2 mm electrodes (100 m/s) and therefore it was decided to use a length of 2 mm for the TW electrodes.

Hamid et al. [32] found that the use of 6 RF and 5 DC electrodes as shown in Figure 2.13 provides effective RF confinement. A smaller number of electrodes made the ions more sensitive to the guard electrode potential, but a larger number did not improve the performance much. Since a larger number of electrodes results in a less compact design and larger fabrication costs, it was concluded that 6 RF electrodes is the best choice. These 6 RF electrodes are then accompanied by 5 arrays of TW DC electrodes.

3.5.2 PCB Design

The PCB design was developed taking all the things mentioned above into consideration. 6 RF electrode strips with a width of 0.50 mm will be alternated by 5 arrays of TW electrodes that also have a width of 0.50 mm each. Although the guard electrode potential influences the ion confinement, its specific width was not of significant importance to be investigated. In the study of Hamid et al. [31] a width of 5.08 mm was used, but it was decided to set the width for convenience to 5.00 mm. Spacing between all electrodes was set to 0.15 mm. This means that the total width of the electrode structure became 17.30 mm. The total width of the PCBs was set to 75 mm, to have enough space for the connectors to the electrical wires and for the screw holes to mount the PCBs. To keep as close to the design of the study as possible, the set of eight TW electrodes was repeated eighteen times, as in the paper. All TW electrodes were set to a width of 2.00 mm with a separation of 2.00 mm, resulting in a total length of 309.45 mm. Since Eurocircuits could fabricate PCBs on which the copper can be applied up to 0.250 mm from the board edge [42], and the first and last TW electrodes were extended with 1.00 mm to 3.00 mm to reduce the unguided path length for the ions, a total PCB length of 311.95 mm was obtained.

The design for the PCBs was created with Sprint-Layout 6.0. This software allows designing and

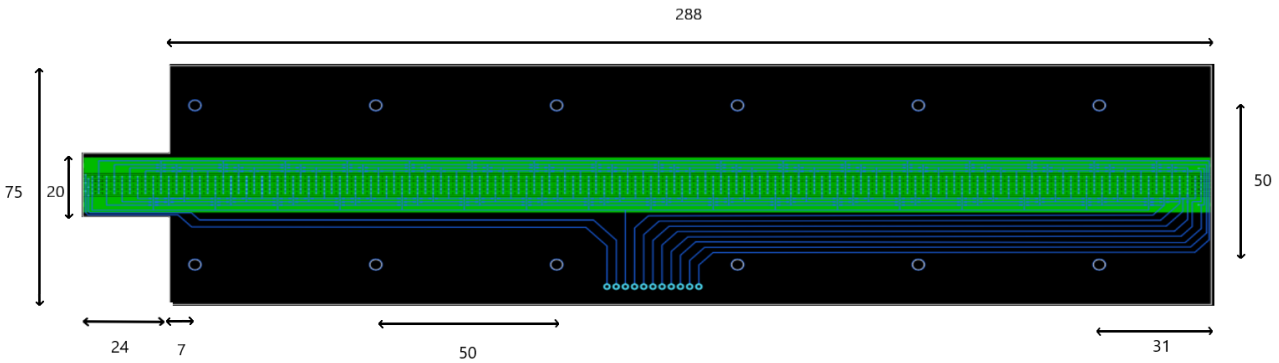

Figure 3.11: Schematic of the PCB including the measurements. The electrodes are depicted in green, while the paths between connectors and electrodes are shown in blue.

editing printed circuit board layouts while providing the means to create single-sided, double-sided, or multilayer PCB [45]. Figure 3.11 shows the PCB design, where the electrodes are indicated in green. This design is for a single PCB, but the opposite PCB is identical, albeit mirrored. The width at the left side is reduced to 20 mm, to form a tip with a length of 24 mm that extends the PCB into the opening between the IFT and main chamber. In this way, ion losses due to diverging ions are reduced. Figure 3.11 also shows 12 holes for mounting the PCBs to the underlying supporting frame. The holes have a diameter of 3 mm, to fit M3 threads and are distanced 50 mm from each other. In this way vibration of the board is kept at a minimal.

The electrode pattern is rather complex. The TW electrodes must be connected to the correct ones (electrode 1 to the next electrode 1, 2 to 2, etc.), without being in contact with the others. A path from the connector to each individual electrode was made, which means that paths are crossing each other. Ideally, this is solved by placing the path of each distinct electrode type in a different layer. This means that the PCBs would exist out of at least 9 layers, where one layer is reserved for the actual electrode pattern and the other 8 layers account for the 8 TW paths (the RF and DC guard electrodes paths can be placed around the TW path and hence a separate layer for these would not be necessary). However, the Sprint-Layout software only provides PCB designs up to 4 layers, which means that we still have to deal with crossings. Thereby, using more layers results in higher fabrication costs. As this PCB is only a first design and will act as a guinea pig to see if we can obtain a signal in the first place, the multilayer idea was discarded. In consultation with a PCB expert, it was decided to solder bridges of so-called 0-Ohm resistors on the 2-layer boards instead [46]. In this way, the paths to the different electrodes are not in contact with each other. The resistors are very small and are soldered onto small solder pads. A detailed image of the electrode structure including the paths and solder pads is shown in Figure 3.12. Since the TW pattern consists of 8 electrodes that repeat 18 times, a lot of bridges are needed.

Due to their complicated design, fabrication of the PCBs by Eurocircuits, as originally planned, would become rather expensive (about 500 euros). Instead, it was chosen to order the boards at the firm JLCPCB that could produce them for a fraction of the price. Thereby, the company is able to produce boards consisting of up to 6 layers [47], which comes in handy when dealing with the serpentine path

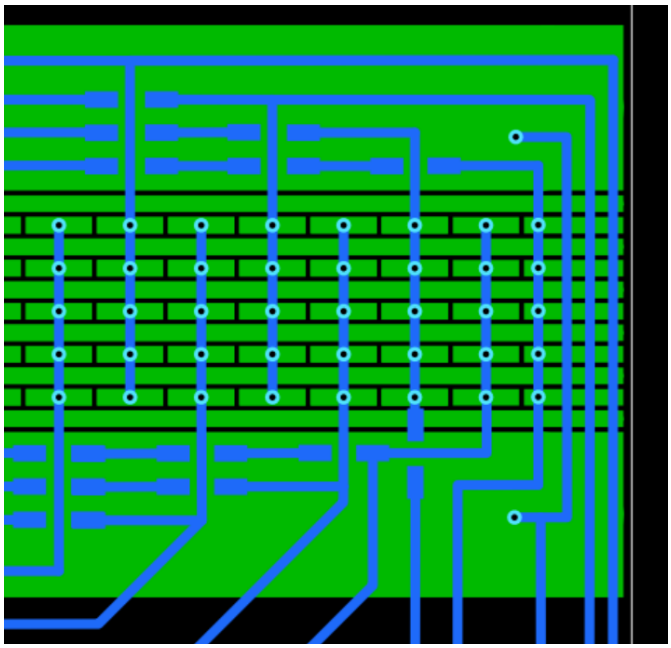

Figure 3.12: Zoomed-in schematic of the PCB design where the last 8 TW electrodes of the PCB are shown. Electrodes are depicted in green and the spacing between them is shown in black. The blue rectangles indicate solder pads.

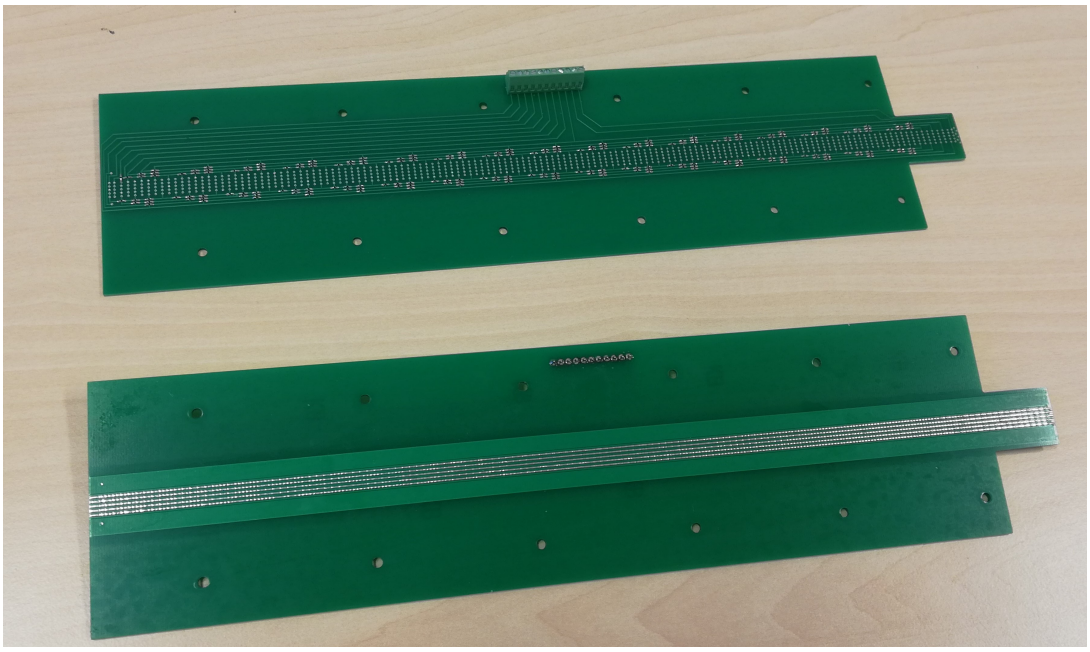

Figure 3.13: Picture of the front and backside of the PCB. The top plate (front) shows the 205 0-Ohm resistors that have been soldered to the PCB manually, as well as the screw connector. The bottom plate (backside) contains all the necessary electrodes and is the side the ion beam is facing.

and switch in the future. The 0-Ohm resistors (type 0402 (1005M)) for our first PCBs were fabricated by Vishay and have a length of only 1 mm [48]. A total of 410 resistors were soldered on the boards manually, using a microscope. For our relatively simple prototype, applying this bridge-technique was manageable, but since a future design would need many more resistors, using multiple layers is a must. Luckily JLCPCB can provide in this need.

To connect the boards to the electronic devices that provide the necessary RF and DC signals, so-called screw connectors were soldered to the boards. Then wires were placed in the screw holders and screwed tight. In this way, wires can easily be attached and removed. At first there was a concern if the material of these connectors would be suitable in the vacuum chamber, as there will be degassing. However, since pressure is relatively high, this was assumed to have no to negligible impact.

3.5.3 Mounting the PCBs

The PCBs were mounted at such a height that ions released from the front chamber enter in the middle in between the boards. To do so, Klaas designed an aluminium supporting construction. Ions enter the main chamber at a height of around 65 mm from the floor of the chamber. The PCBs themselves are about 1.5 mm thick and are typically spaced by a gap of 2-5 mm (depending on the strength of the RF and DC signals) [31] [32] [44] [34]. This requires the bottom board to be at a height of about 60 mm from the floor. For this, an aluminium construction consisting of two long parallel beams with each 2 feet was designed. The feet were mounted on the bottom of the chamber, in which threaded holes had been tapped exactly for this purpose. In the initial design, the feet were short, leaving some screw holes in the floor empty. For better support, it was decided to extend the feet and fix them on the bottom chamber plate at two locations. Another 10 mm height was added by means of 12 narrow ceramic tubes that are standing in a pillar-like fashion. These tubes were placed around M3 thread tapped into the aluminium beams and were distanced according to the hole pattern on the PCB. The bottom PCB was placed on these pillars. The supporting construction is shown in Figure 3.14.

The gap between the two PCBs is also of importance. There must be enough space for the ions to

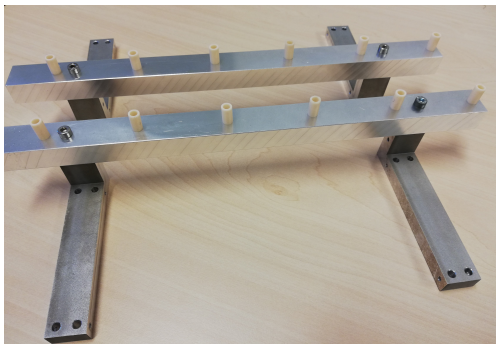

Figure 3.14: Aluminium construction supporting the PCBs. It consists of 2 parallel beams that are mounted on the chamber floor by means of 4 long feet. 12 ceramic pillars are placed on the beams to heighten the position of the PCBs even more.

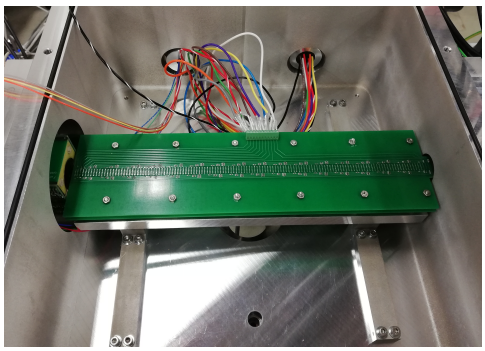

Figure 3.15: The whole SLIM construction consisting of the supporting frame, the spacers and the PCBs, mounted in the main chamber. The boards are screwed onto the parallel aluminium beams and are separated by ceramic washers.

travel, but if the distance between plates is too much, the strength of the electric fields becomes too small to drive the ions. Fortunately, this strength is tunable, such that to a given spacing the best matching RF and DC signal strengths can be found. 4 mm thick ceramic washers were used to separate the two PCBs. The boards, together with the ceramic tubes and washers were mounted on the aluminium supporting frame by M3 thread and were tightened by nuts. Figure 3.15 shows the whole construction installed in the main chamber. By splitting the electrical wires, signals to both top and bottom board can be applied.

3.6 Quadrupole

The TW-SLIM is coupled to the existing mass spectrometer by connecting the back side of the RIF chamber to the octupole chamber in the existing setup. Pressure in these two chambers differs by 4 orders of magnitude, which is too much to maintain via differential pumping. Therefore an additional

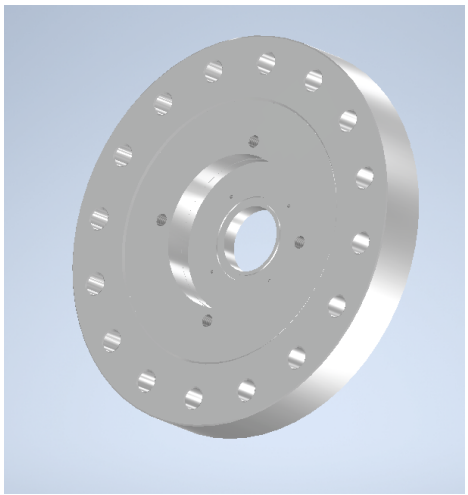

Figure 3.16: Design of the back flange of the quadrupole that is to be welded to the vacuum chamber.

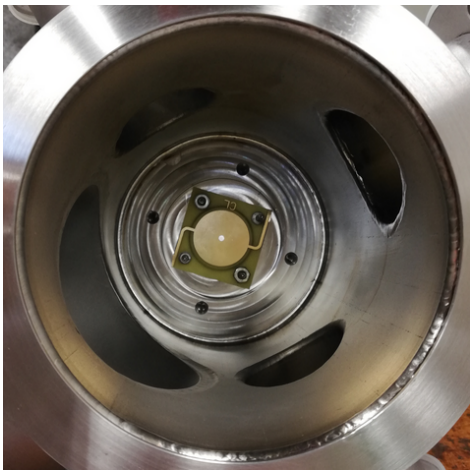

Figure 3.17: Diaphragm plate mounted to the backflange at the inside of the quadrupole chamber.

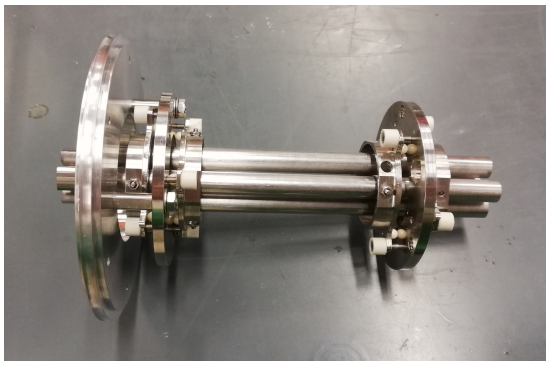

Figure 3.18: Picture of the adapted quadrupole such that it fits into the vacuum chamber.

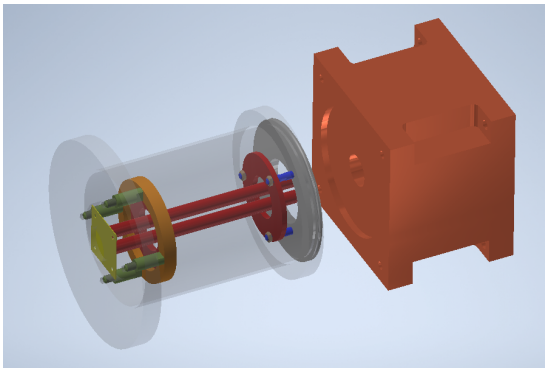

Figure 3.19: Schematic of the quadrupole (red rods) placed in the orange holder. Also shown is the RIF chamber, to which the quadrupole chamber is connected.

small chamber was placed between the RIF and octupole chambers. This chamber reduces the pressure after the RIF and also acts as a transition from the KF flanges used in the SLIM system to the CF ones used in the existing mass spectrometer setup. An existing vacuum chamber was modified to house a quadrupole, that guides the ions through the chamber. The chamber already accommodated additional flanges to enable connections to the pump, the pressure gauge and wires to deliver the necessary electrical signals to the quadrupole, but it did not have the desired CF back flange. Therefore an altered blind CF-100 flange was welded to the chamber. The design of this flange was created using Autodesk Inventor Professional software [49]. Into the flange, an opening was made to allow the ions to leave the chamber. Thereby, threaded holes for mounting a diaphragm plate as well as for mounting the quadrupole itself were tapped into the flange. Figure 3.16 shows the design of the back flange. A 25.4 mm opening was tapped through which the ions leave the chamber, which is covered by a 2 mm diaphragm. A small gutter was milled around the opening to allow for an O-ring that electrically insulates the diaphragm. The diaphragm plate was mounted by screws to the back flange and a picture of this is shown in Figure 3.17. This arrangement is milled in 11.9 mm as compared to the rest of the flange to get the diaphragm as close to the octupole in the next chamber as possible to reduce ion losses. The four threaded holes in the middle circle serve for mounting the quadrupole, while the holes around the edges are there to connect the flange to the octupole chamber.

To guide the ions through the vacuum chamber, an existing quadrupole was used that was cut to obtain the right dimensions to fit into the chamber. A picture of the cut quadrupole is shown in Figure 3.18. Figure 3.19 shows schematically the way this quadrupole is placed in the chamber. This schematic was made by the workshop using Autodesk Inventor Professional. A holder, mounted on the back flange of the chamber, was made that electrically insulates the quadrupole and supports it at the side of the octupole. This makes the system more user-friendly, since the quadrupole is easily placed in this holder. At the RIF side, the quadrupole is mounted by means of the support disk that was part of the inital quadrupole system. A different modification of the device is that the ends of the rods were polished. In this way, they fit into the hole at the end of the RIF chamber. A picture of the quadrupole chamber mounted between the RIF and octupole chambers is shown in Figure 3.20.

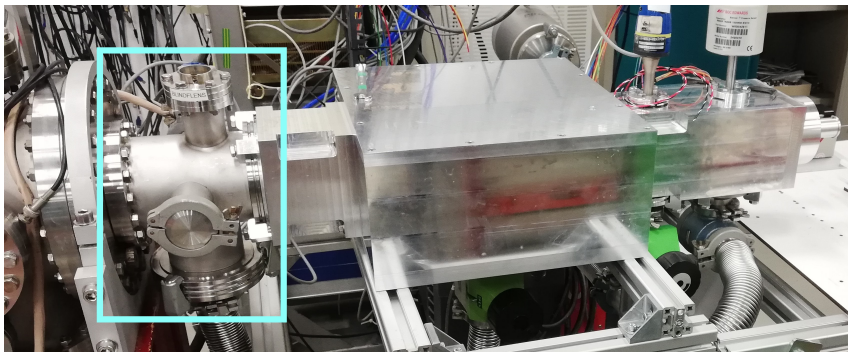

Figure 3.20: Picture of the quadrupole chamber (in the blue rectangle) that connects the RIF (right) to the octupole (left) chamber.

3.7 Multipin Feedthroughs

There are many electronic components within the vacuum chamber system, to which all multiple DC and RF signals need to be brought via wiring. The HPIF and RIF both require 3 DC and 2 RF signals (hence 5 wires in total for each), while the other ion funnel, the IFT, needs a total of 10 wires (8 DC + 2 RF). Thereby, the PCBs require 8 DC signals to the TW electrodes, as well as 1 DC signal to the guard electrodes and 2 RF signals. This is even only the minimal amount of wires needed, as in the future a switch is planned to be implemented, which would require 2 additional DC signals for the switching element. Hence the total number of wires that needed to go into the vacuum system was at least 31. With this many wires, the commonly used single-pin feedthroughs were considered a bad option since they would consume lots of space, be very impractical when connecting and disconnecting and would make the design overly expensive [19]. Therefore it was decided to use multipin feedthroughs instead. To prevent discharges caused by closely spaced pins inside the vacuum chambers, it was chosen to use feedthroughs with multiple wires, in which each wire is sealed individually. These feedthroughs were purchased at the company Pave Technology that, commissioned by us, produced 2 feedthroughs consisting of 9 wires and 2 consisting of 12 wires.

To mount the multipin feedthroughs on the chamber walls, KF-40 feedthrough flanges that fit in the designated holes in the walls, were designed [38]. Figure 3.21 shows these flanges for the two types of

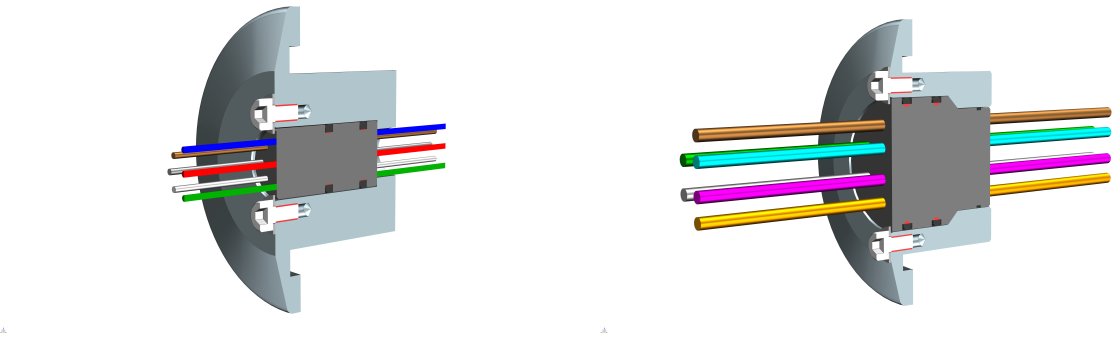

Feedthrough with nine wires Feedthrough with twelve wires

Figure 3.21: Schematics of KF-40 flanges that contain the multipin feedthroughs.

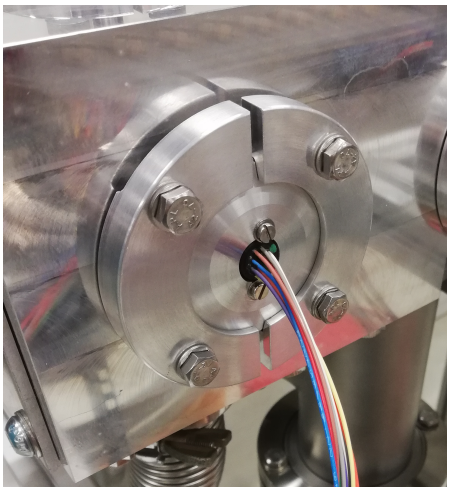

Figure 3.22: Multipin feedthrough mounted on the chamber wall by means of two KF-40 face clamps.

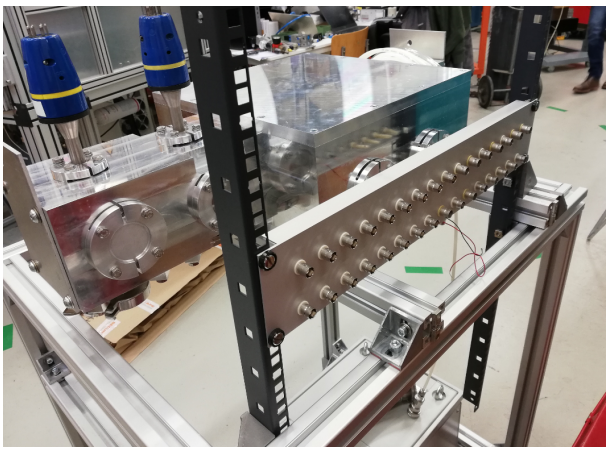

Figure 3.23: BNC connector board in front of the SLIM stage. Wires can be soldered to the back, while BNC cables are connected to the front.

feedthroughs. These particular designs make sure that the connections are vacuum tight. The flanges are tightened to the flat surfaced by means of KF face clamps. Figure 3.22 shows such a tightened flange containing the feedthrough with 9 wires mounted on the chamber wall.

Since there are many wires involved in the system, overview can be lost quickly. To avoid that, a board was made that contains BNC connectors. Wires coming from the multipin feedthroughs were soldered to the back of these connectors. At the front, BNC cables were connected. By labelling the connectors, one easily sees which cable is which. Another advantage is that most of the electronic devices work with BNC connections, meaning that only a BNC cable is enough to connect the desired element to the appurtenant electronic apparatus. Wires can easily be extended by connecting multiple in a row. Figure 3.23 shows a picture of the connector board in front of the front and main chamber. In this picture, the multipin feedthroughs have not been installed yet, but they are placed at the spots that now accommodate the blind flanges.

3.8 Vacuum System

Pressure is key element in the TW-SLIM stage. In order for the TW-SLIM module to function properly and separate ions, the travelling ions should make collisions with buffer gas molecules. This is done by introducing helium into the main chamber. A relatively high pressure is therefore needed in this chamber. In their study, Hamid et al. [31] can operate the SLIM system successfully at a pressure of 5.3 mbar (4.0 Torr), and therefore it was decided to use this pressure as well in our system as a starting point. This is however not the only place where the role of the pressure is important; in the other chambers it must be well considered as well.

As already discussed, a high pressure is needed in the HPIF chamber such that a large number of ions can be brought into the system. In this chamber, pressure is the highest, with a value of 10-15 mbar. The pressure in the IFT chamber is lower than in the HPIF chamber and even slightly lower than in the main chamber. A small differential positive pressure between TW-SLIM and ion funnel trap namely effectively prevents solvent and contaminants from entering the TW-SLIM module [31]. In their study, Hamid et al. [31] use a pressure difference of 5 mTorr ($\approx$ 0.1 mbar) between the IFT and TW-SLIM. Since the TW-SLIM will probably operate at around 5.3 mbar, this means that the pressure in the IFT chamber must be 5.2 mbar. The RIF chamber is open to the main chamber and hence has the same pressure (5.3 mbar).

The quadrupole chamber provides the transition from the relative high pressure in the main chamber to the much lower pressure (around 10^{-4} mbar) in the octupole chamber in the existing setup. Pressure in this chamber should therefore be somewhere in the 10^{-2} mbar range. The most suitable pressure will be found when doing the first experiments. This also applies to the pressures in the other chambers mentioned above.

For reasons of cost-efficiency, the chambers are not pumped by individual pumps. Thereby, the more elements in a system (e.g. pumps), the larger the possibility of trouble anywhere in the system. Therefore chambers are coupled to the same pump. In his project, Klaas already tested that this is possible [19]. Our system is slightly more complicated, since more chambers (HPIF, IFT and main) are connected to the same pump than investigated previously. Three screw valves are used to control the pressures in the individual chambers. To provide the necessary pressures, a powerful Edwards EH Mechanical Booster pump is used, in combination with a backing Edwards E2M80 Rotary Vacuum pump. The pressures are monitored by Pfeiffer pressure gauges. Since there are already three elements coupled to the mentioned pumps, the quadrupole chamber uses a different pump, namely a scroll pump. With this setup, it is possible to obtain the desired pressures in the different chambers.

Chapter 4

Experiments

After the design of the TW-IMS stage was completed and all parts were assembled together, it was time for some first actual experiments. In first tests, it was studied if it was possible to drive ions through the different elements. In this chapter, these experiments and their results are presented. Ultimate goal is to connect the stage to Paultje, but before that step is reached, the system had to be tested on its own. The solution used for these tests consisted of 50 μmol leucine enkephalin in methanol, to which 1% of an acid was added. Due to the acid, charged ions were obtained that then were driven through the system.

4.1 Testing HPIF

The logical first step in testing the TW-SLIM stage was to focus on the the first ion funnel, the HPIF. Only to this funnel RF and DC voltages were applied, while all other elements were kept off. To measure how many ions moved through the funnel, the CL plate of the HPIF was used. When ions hit this plate, they transferred their charge to the metal. An electric current proportional to the number of impinging ions was then measured by a Keithley 6485 picoammeter.

4.1.1 Fixed Settings

The signals to the funnel are controlled by the MIPS device. The auto-tune functionality was used to optimize the RF frequency to 289 kHz, which was kept constant. What we did tune was the RF peak-to-peak voltage V_{pp} to explore its influence on the ion signal. This was controlled via the RF drive level. Furthermore, the potentials applied to the needle, the capillary and the first and last electrode of the funnel were found to play a role, as well as the temperature of the capillary and the pumping speed of the syringe. In ESI experiments it is common to work with needles at voltages of around 3 kV, so this was the first bias we tested with.

At first we tried to find the optimal DC biases. The capillary was set to 70 °C, while the syringe sprayed the solution to the needle at a flow rate of 60 μL/h. We varied the voltages to firstly obtain a signal and after that we made small variations in order to improve this signal and find the maximum value. It turned out that the best signal was obtained when 220 V was applied to the capillary and 250 V and 120 V to the first and last electrodes (HPIF in and out), respectively. These values were used throughout the other tests.

4.1.2 Results

After the optimal DC potentials were found, the behaviour of the signal as a function of temperature, pressure, RF peak-to-peak voltage and flow rate was investigated.

At first the influence of the temperature of the capillary on the ion current was explored. By heating the capillary, remaining solvents were evaporated. This test served to optimize the temperature and

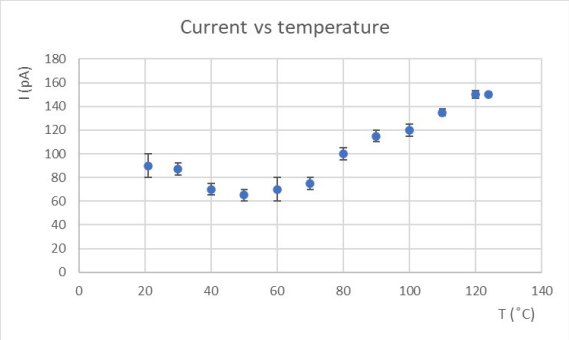

Figure 4.1: Signal at picoammeter as a function of temperature of the capillary at 60 μL/h, 0.6 mbar and 21 V_{pp}.

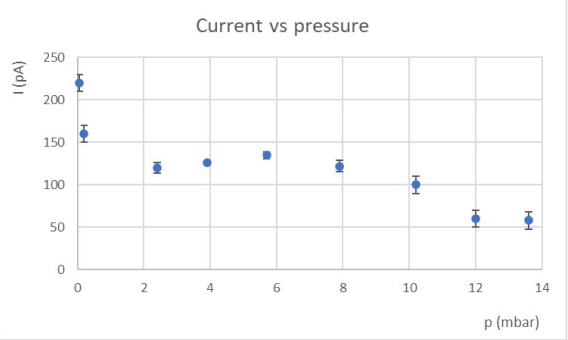

Figure 4.2: Signal at picoammeter as a function of the pressure in the HPIF chamber at 60 μL/h, 119 °C and 21 V_{pp}.

was performed at a flow rate of 60 μL/h, pressure of 0.6 mbar and an RF peak-to-peak voltage of 21 V_{pp}. Figure 4.1 shows the results. The ion current displayed on the picoammeter was varying constantly within a certain range and the error bars indicate up to which values this occurred. Starting at room temperature, 21°C, the current slightly decreased, until at 70°C it stared to increase. This dip could be caused by external influences such as fluctuations in the amount of ions that were brought to the needle or to a sudden increase in air that flows between the needle and the capillary. Nevertheless, this dip is relatively small and therefore it was assumed that temperatures in this range did not have much influence on it. After the dip, the temperature increased and at high values, the signal gives the impression to saturate at about 150 pA. This suggested that the solvent was evaporated fully and using a higher temperature would not give an added value. Because of this and the fact that it takes a much longer time to reach higher temperatures, we decided to stop measuring at a temperature of 124°C and take 120°C as the optimal temperature for further experiments.

The next test we performed was changing the pressure in the HPIF chamber, while flow rate, temperature and RF peak-to-peak voltage were kept constant at values of 60 μL/h, 119 °C and 21 V_{pp} respectively. The results are shown in Figure 4.2. In the first measurement, the valve between pump and chamber was fully open, such that pressure was at its minimum (below 0.1 mbar). The pressure gauge used here did not operate at such a low pressure and therefore we can only give an upper limit for the pressure. From the plot it can be seen that the maximum signal was obtained at the lowest pressure and had a value of about 220 pA. Upon increasing the pressure then, the ion current decreased. A local maximum was found near 6 mbar, which was presumably caused by fluctuations in the ion concentration in the solvent. This could have been prevented by mixing the solution better. The overall trend however shows that the ion current decreased when the pressure was increased. A simplified explanation for this is that at higher pressures more collisions occur and less ions make it straight through the funnel, albeit that at our "lower pressures" there are already many collisions.

The third test that was performed was to check the impact of the flow rate at which the solution containing the biomolecules reaches the ESI needle. Although from the previous test we concluded that highest ion current was obtained at lowest pressure, in this test a high pressure of 9.6 mbar was used, since in combination with the second funnel an operating pressure of 10-15 mbar was expected. Here the lower limit was taken to obtain the best signal in this range. We were not able to exactly reach 10 mbar, since the valve could not tune that precisely, but this value sufficed. As can be seen in Figure 4.3, there was only a small increase in signal when the flow rate became larger. Of course it will drop down to zero when reaching a rate of 0 μL/h, since then no particles are brought into the system, but for higher rates the signal does not show signs of being influenced significantly. This means that we can test already at low flows and obtain a nice signal, which is a positive thing, since samples are often expensive and in this way less of it will be needed.

Lastly, the RF peak-to-peak voltage was investigated at different pressures. Measurements of the ion

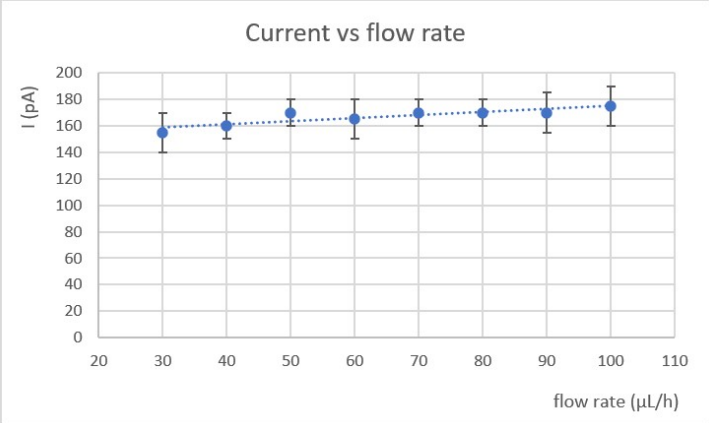

Figure 4.3: Signal at picoammeter as a function of the flow rate through the needle at 119°C, 9.6 mbar and 21 V_{pp}.

current for these voltages at four distinct pressures are shown in Figure 4.4. The <0.1 mbar indicates that the valve was fully open and the pressure was too low to measure. Above 4.0%, the signal decreased with the same trend at all the different pressures. At smaller voltages, all the currents, except at the lowest pressure, stayed more or less constant. Why the signal at this lowest pressure shows its specific trend is not understood and more experiments could be done to investigate this behaviour. However, since the purpose of the HPIF is to operate at high pressure and due to limited time, this was not investigated further in this project.

We now know how to obain the largest ion current at the end of the HIP. A summary of the results to reach this signal at the picoammeter is shown in Table 4.1. These values are used as a stepping stone for the next experiments.

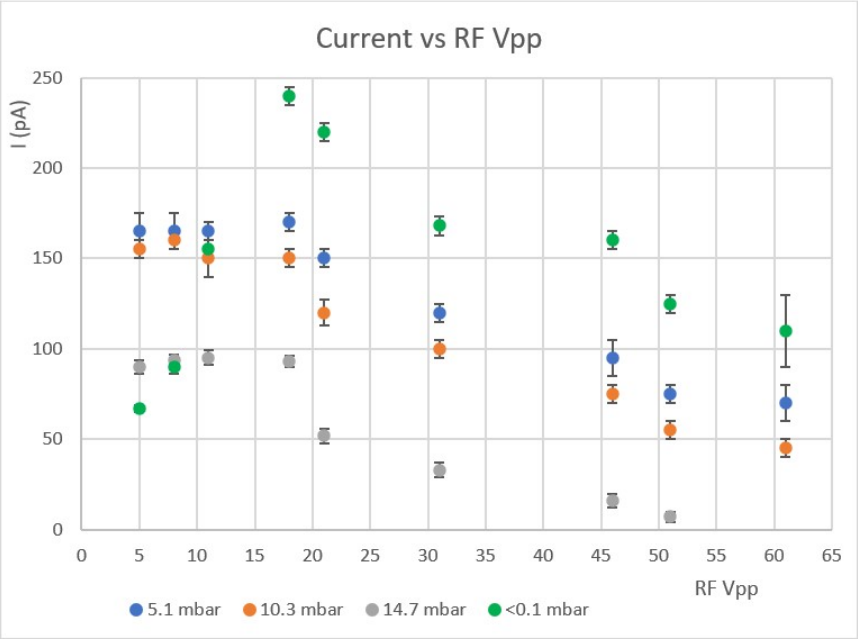

Figure 4.4: Signal at picoammeter as a function of V_{pp} for different pressures at 60 μL/h and 119°C.

Parameter	Value
Bias needle	3.087 kV
Bias capillary	220 V
Bias HPIF in	250 V
Bias HPIF out	120 V
Temperature	120°C
Pressure	<0.1 mbar (valve fully open)
Flow rate	Anything above 30 μL/h
Drive frequency	289 kHz
RF V_{pp}	18 V

Table 4.1: Values of parameters in HPIF to obtain the best signal.

4.2 Testing HPIF + IFT

After testing the first funnel, we investigated if ions passed the IFT funnel as well. This was tested by placing a Faraday Cup behind the IFT at the place where ions enter the main chamber. In this case, the ”cup“ is a small isolated metal plate that was mounted on a supporting plate that was fixed to the chamber floor, see Figure 4.5. Its design was improvised and based on existing parts.

The Faraday cup was connected to the picoammeter through a BNC feedthrough that was installed at the flange that facilitates the helium inlet. At first, one of the wires of the multipin feedthroughs was used, but this wire picked up RF signals from the other wires in the feedthroughs and therefore could not supply a measurable signal. This problem was solved by using the BNC feedthrough.

4.2.1 Fixed Settings

As in the tests with HPIF, the experiment started by finding the optimal DC biases. This time it was more challenging since there were more voltages involved. We knew from the previous experiments which settings would give most signal through the first funnel and these were used as a starting point. Since both funnels have the same length, the voltage gradient found in the first funnel was used in the second one as well. Due to the trap function of the IFT, the electrodes responsible for that had to get their own biases. These were estimated based on their position in the funnel, such that the voltage gradient was preserved. Based on these starting conditions, the signal was optimized. An optimal RF frequency of 811 kHz was found, as well as the bias voltages displayed in Table 4.2. Note that the trap function has not been put to work yet. Since the optimal temperature and flow rate were already found in the previous HPIF experiments, these parameters were not investigated in the upcoming experiments, but

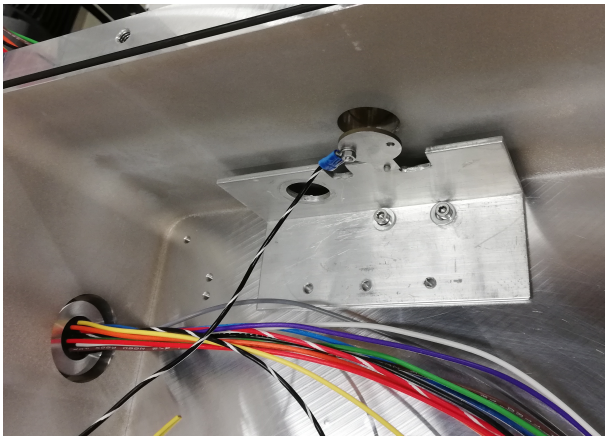

Figure 4.5: Faraday cup placed at the entrance to the main chamber to detect an ion signal.

Element	Voltage (V)
Needle	3420
Capillary	265
HPIF in	382
HPIF out	230
HPIF CL	229
IFT in	100
IFT trap in	30
IFT grid 1	31
IFT grid 2	22
IFT grid 3	20.4
IFT trap out	15.8
IFT out	10.4
IFT CL	8.6

Table 4.2: Values of biases for HPIF and IFT to obtain the best signal.

rather stayed constant at values of 120°C and 60 μL/h respectively. It turned out that using the biases as shown in Table 4.1 did not result in the best throughput of ions. With higher voltages for the needle, capillary and in the HPIF, signal at the HPIF CL plate improved up to 500 pA, which is more than two times as much as the largest signal measured in previous experiments. However, the voltage gradient remained similar, suggesting that this gradient is optimal.

4.2.2 Results

After finding the optimal DC biases, the first thing that was explored was the pressure dependence of the ion beam. This experiment was carried out at 280 V_{pp} and 215 V_{pp}, for the HPIF and IFT respectively, since these values gave the best signal.

Firstly the pressure in the HPIF chamber was varied, while the valve to the IFT chamber was kept untouched. The resulting behaviour of the current detected by the picoammeter is shown in Figure 4.6. The largest signal, with a value of 170±8 pA, was obtained at a pressure of 19 mbar. One thing that was observed while running this experiment, was that the pressure in the IFT chamber changed significantly when the pressure in the HPIF was varied. This is due to the relative large opening between the two chambers, which allows for indirect pumping of the IFT chamber. The way the pressure in this chamber depends on the pressure in the HPIF chamber is shown in Figure 4.7. As can be seen, the pressure in the IFT chamber scales approximately linearly with the one in the HPIF chamber. At a pressure of 19 mbar in the first chamber, the IFT pressure was close to 4 mbar, suggesting that around this value the signal is optimal.

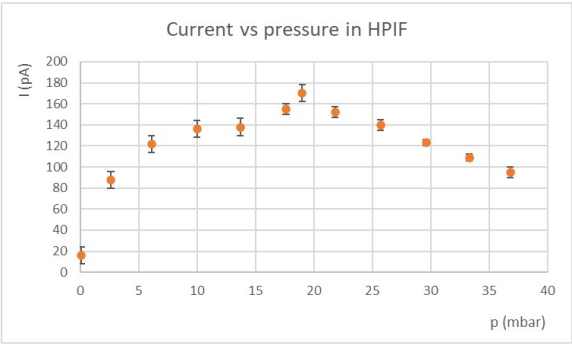

Figure 4.6: Signal at picoammeter as a function of pressure in HPIF chamber at 60μL/h and 120°C.

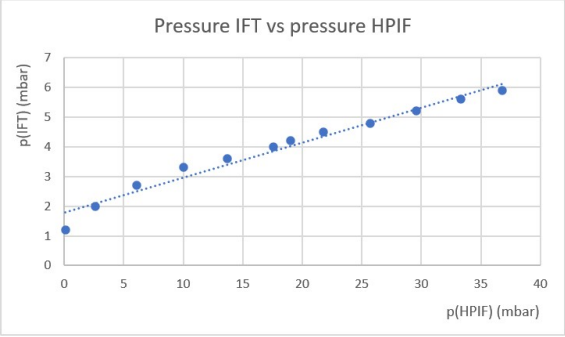

Figure 4.7: Pressure in IFT chamber as a function of pressure in HPIF chamber

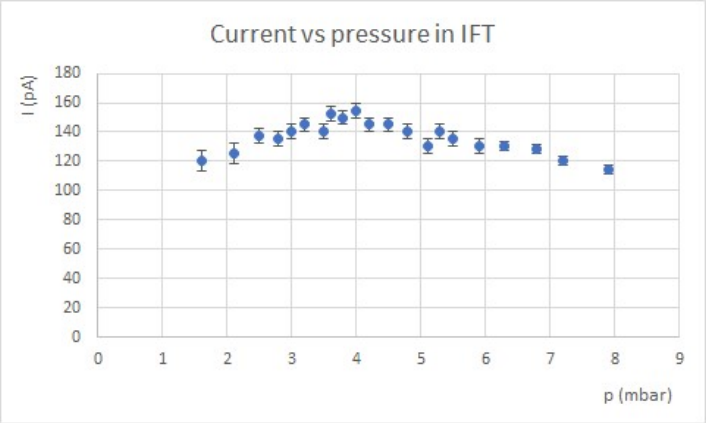

Figure 4.8: Signal at picoammeter as a function of pressure in IFT chamber at 60μL/h and 120°C.

This is indeed what was measured. Figure 4.8 shows the current as a function of the pressure in the IFT chamber, when the pressure in the HPIF chamber was 19 mbar. A maximum was found at 4.2 mbar. You can see that the system is very sensitive to changes in pressure, since differences up to 40 pA were obtained over a pressure range of a few mbar. The pressure in the HPIF chamber was not noticeably influenced when the IFT pressure was changed. In both Figures 4.6 and 4.8 the error bars become smaller when pressure increases: the larger the pressure, the more stable the signal becomes. This behaviour was not observed when testing the HPIF on its own, as can be seen in Figure 4.2. This might be due to the fact that the voltage settings were not optimal in that experiment.

After finding the optimal pressures, the RF peak-to-peak voltages were investigated. As already briefly mentioned, much higher voltages than in the case of HPIF alone were needed to obtain a detectable signal. The RF heads used to create the RF signals can handle a maximum power of 10 W, which is reached at a V_{pp} voltage of about 280 V. The suitable V_{pp} and corresponding power are very sensitive to the pressure. The higher the pressure, the larger the V_{pp} voltage to obtain a signal. At the same time, the power at a certain voltage decreases when the pressure becomes higher. The high pressure in the HPIF chamber was such that the maximum allowed power was not reached, but the lower IFT pressure provided a risk of exceeding the limit. Therefore at first the RF peak-to-peak voltages of the IFT were investigated. The resulting signal upon changing these voltages is shown in Figure 4.9. In this experiment, the V_{pp} voltage of the HPIF was set to 280 V. The optimal IFT V_{pp} was found to be 130 V. At this value then, the influence of the V_{pp} voltage of the HPIF on the detected signal was

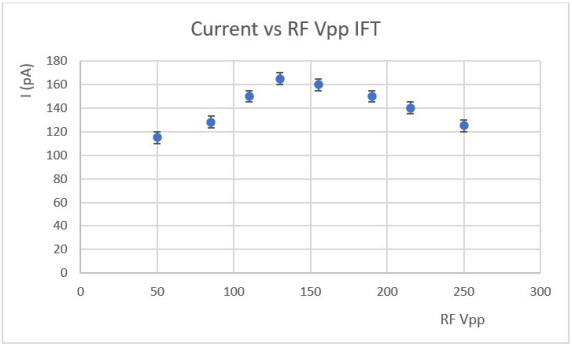

Figure 4.9: Signal at picoammeter as a function of V_{pp} of IFT at constant HPIF V_{pp} of 290 V.

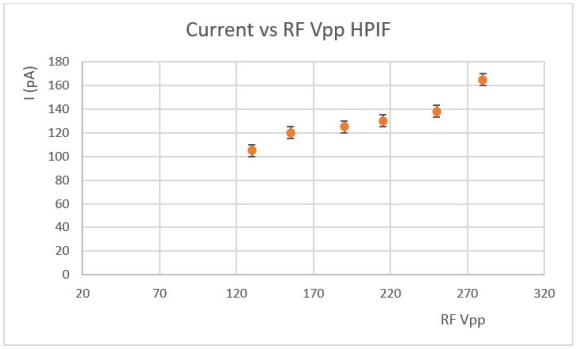

Figure 4.10: Signal at picoammeter as a function of V_{pp} of HPIF at constant IFT V_{pp} of 130 V.

Parameter	Value
Temperature	120 °C
Pressure HPIF	19 mbar
Pressure IFT	4.2 mbar
Flow rate	Anything above 30μL/h
Drive frequency HPIF	829 kHz
Drive frequency IFT	811 kHz
RF V_{pp} HPIF	280 V
RF V_{pp} IFT	130 V

Table 4.3: Values of parameters for HPIF and IFT to obtain the best signal.

explored and this is displayed in Figure 4.10. It turned out that a HPIF RF V_{pp} voltage of 280 V gave the optimal signal. Table 4.3 summarizes the values of the different parameters to obtain the best signal at the Faraday cup.

Now that is shown that ions can pass the first two funnels, the trap function was put to work. By setting a pulsing voltage to the Grid 3 electrode of the IFT, we were able to block the signal for a specific time. The pulsing was done by switching at predefined times between a lower and a higher voltage such that the ions were let through or blocked respectively. The timing scheme of this pulsing can be seen in Figure 4.11, which shows that the trap was on for 46 ms and off for 18 ms. During the off-state, ions were released from the trap, leading to an ion signal at the Faraday cup. This was monitored with an Agilent Technologies DSO6034A oscilloscope and its display is shown in Figure 4.12. The white line denotes the signal from the Faraday cup and it follows nicely the pulses imposed on the electrode in the IFT, that is displayed in pink. When the voltage of Grid 3 was increased from 20.4 V to 60 V, the ions were blocked and the measured signal reduced from roughly 175 mV to 0 V.

The pulse height and width could be adjusted manually and the ion signal responded to it as expected, which was visible both on the oscilloscope as well as on the picoammeter. When for example the trap was on for 2/3 of the time, the signal measured by the picoammeter decreased to 1/3 of the value of when the trap was off. The picoammeter was too slow to measure the individual pulses, but rather gave an average. Hence when ions were blocked for 2/3 of the time, 1/3 of them made it through the funnel on average, leading to a signal that was 1/3 of its initial value when the trap was off.

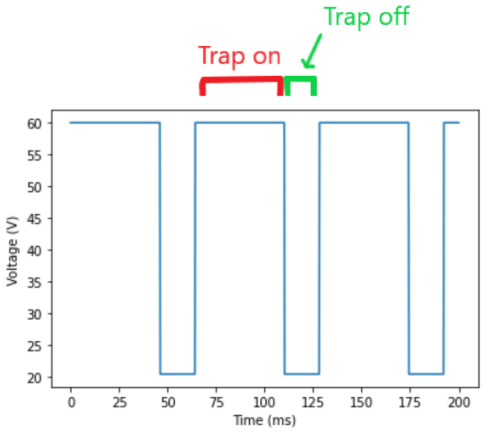

Figure 4.11: Timing scheme of the ion trap with on the y-axis the bias applied to electrode Grid 3 of the IFT.

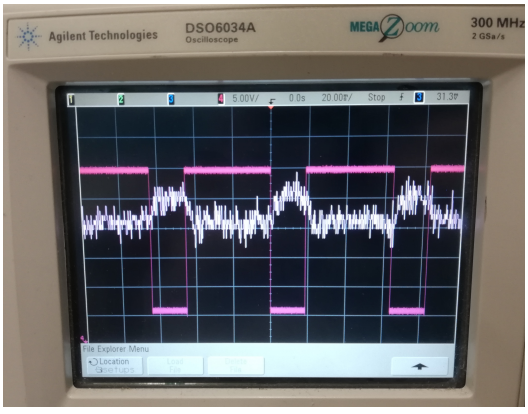

Figure 4.12: Display of oscilloscope showing the voltage pulses imposed on grid 3 (pink) and the resulting signal at the Faraday cup (white).

4.3 Testing TW-SLIM module

Once it was shown that ions could reach the TW-SLIM module, it was time to explore the settings to drive them through this module. The position of the Faraday cup was changed to directly behind the PCBs. This means that we could not check any longer if ions were actually arriving at the module in the first place. What could be measured however, was the throughput of ions through the HPIF, by connecting the picoammeter to the CL plate of this first funnel. For all upcoming tests this was always step one. After making sure that a signal was found at this position, the detector was connected to a Faraday cup that was placed behind the PCBs (but in front of the RIF), as shown in Figure 4.13. For the HPIF and IFT, the settings as described in the last section were used.

4.3.1 Fixed Settings

At first the RF frequency and peak-to-peak voltage, as well as the guard bias were determined. This was done without the travelling waves. Temperature of capillary was set to 120 °C and flow rate to 60 μL/h, while pressure in the main chamber was kept at 2.0 mbar. Optimal RF frequency and V_{pp} were found to be 2.115 MHz and 370 V respectively. The pressure and V_{pp} values here were just a starting point and were explored in separate follow-up tests. The guard voltage gave the best signal at a value of 3.0 V in combination with an offset of 17 V, meaning that the actual value of the guard voltage was 20 V.

4.3.2 Results

In the first test, influence of the pressure on the signal was explored. For this, no travelling waves were applied, hence solely RF and guard voltages. Thereby, the test was performed without letting helium into the system. The lowest pressure that could be obtained in our setup was 0.8 mbar, which was our starting point. Settings as mentioned above, as well as pressures of 18.9 mbar and 3.8 mbar in the HPIF and IFT chambers respectively, were used and the results are shown in Figure 4.14. An optimal signal of 100 pA was reached at a pressure of 1.5 mbar. This is a fairly broad maximum, meaning that little changes in this pressure range do not influence the signal much. With the used settings, the signal after the first two funnels should be around 170 pA, suggesting an ion throughput through the TW-SLIM module of almost 60%. However, since we could not measure the exact signal in front of the module within this experiment, this is an estimate. The 170 pA was the maximum value obtained, so it is more likely that less ions arrived at the module in the first place, which would increase the throughput percentage.

At a pressure of 1.4 mbar in the main chamber then, the impact of the RF frequency and peak-to-peak voltage was investigated. The signal did not change much when RF frequency was varied in the

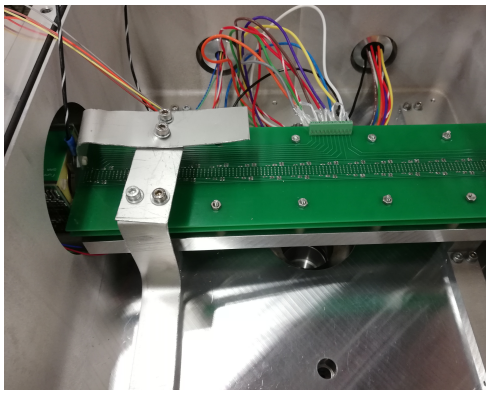

Figure 4.13: Construction for the Faraday cup placed at the end of the PCBs (at the left of the picture).

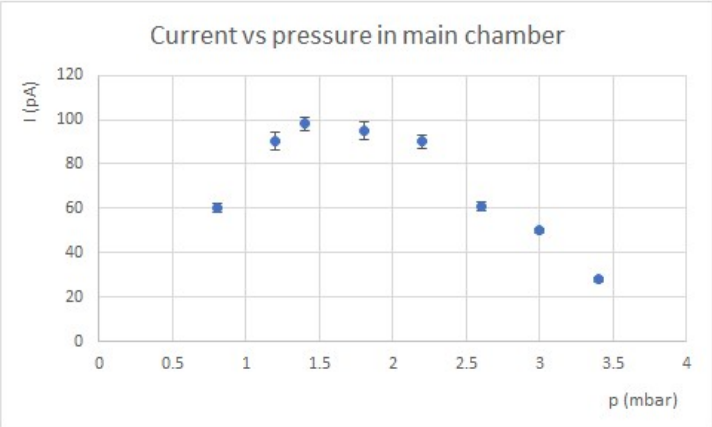

Figure 4.14: Signal at picoammeter as a function of pressure in main chamber.

range of 2.1-2.2 MHz. Outside this range, the signal decreased noticeably, indicating that we were out of resonance. Upon increasing the frequency in the mentioned range, the peak-to-peak voltage increased as well, but by adjusting the drive level, the same optimal signal as at the other frequencies was obtained. Since the exact RF frequency did not have a significant effect on the signal, the rest of the tests were performed with the same settings as in the pressure test, i.e. at a frequency of 2.115 MHz and 370 V_{pp} voltage.

With these optimal settings, the travelling waves function was turned on. The MIPS device was set to TWAVE mode, to generate 8 repetitive blockwaves that are each phase shifted by 45 degrees. The 8 outputs were connected to the 8 consecutive electrodes patterned on the PCBs. In order to function correctly, the trap was put to work, by sending 20 ms pulses at a frequency of 5 Hz. This means that the ions were trapped for 90% of the time, while the other 10% they were let through. This is schematically shown in Figure 4.15.

While doing this test, a constant flow of helium buffer gas was introduced into the system, such that the pressure in main chamber rose up to 2 mbar. The signal at the Faraday cup was monitored with an

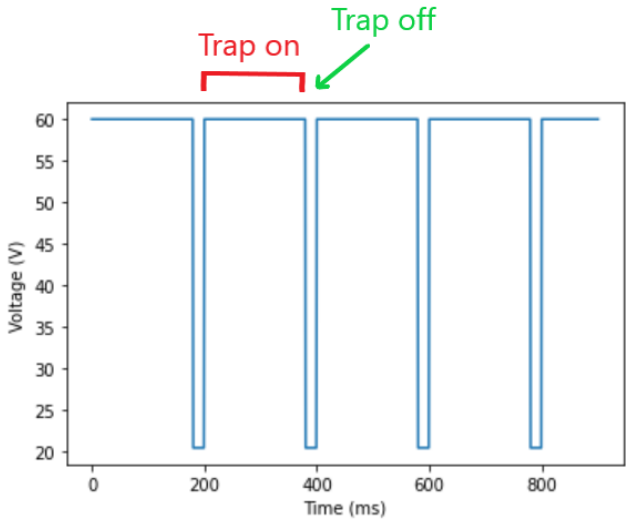

Figure 4.15: Timing scheme of the ion trap for the TW test with on the y-axis the bias applied to electrode Grid 3 of the IFT.

oscilloscope, to monitor the response of the signal when ions are being trapped for a certain time. As a first guess, the frequency of the travelling waves was set to 20 kHz, which resulted in a travelling wave velocity of 3 m/s. At this relative low TW velocity, peak widths will be small, since ions are expected to be confined to travelling traps. Their mobilities allow them to keep up with the wave velocity and hence the effects due to diffusion are constrained [31]. This low velocity was therefore considered a good starting point. The peak-to-peak voltage was increased from 0 V until a signal was found. A maximal signal was obtained at a value of 20 V. Since to all output voltages of the MIPS device an offset voltage of 17 V was applied, this means that the blockwave was varying between 7 V and 27 V. To improve this signal, pressure in the main chamber was increased. Figure 4.16 shows a picture of the oscilloscope displaying the signal behind the TW-SLIM module at a pressure of 4 mbar. Like in Figure 4.12, the trap voltage is displayed in pink, while the signal of ions arriving at the Faraday cup is shown in white, but now the trap is open at the moments the pink signal goes up instead of down. It can be seen that the signal nicely follows the pulses applied to the trap. One has to keep in mind however that the pulsing and travelling waves have not been synchronized yet. When doing so, the signal presumably will increase significantly. Nevertheless, even without synchronization clear sharp peaks are visible, that appear at the moments the trap is turned off. If one looks closely, different small peaks can be identified within the large peak, that recur at the same position each time the trap is switched off. This indicates that there is some kind of separation of ions, possibly due to differences in mobility. This should be verified with a mass spectrometer, since according to Hamid et al. [31], the TW speed should be too low to achieve significant IMS separations. Increasing the TW speed will improve the resolution.

Upon increasing the pressure, the overall signal increased. However, above about 10 mbar, the system behaved very strange: the signal suddenly increased by more than a factor of 10 to values above 1 nA. When blocking the ion beam, this value even increased by a few hundred pA. This odd behaviour could be caused by discharging somewhere in the system in the system and should be investigated in more detail. There are plenty of other tests that should be performed as well, but within the time available of this project these were infeasible. For example, the influence of the different parameters such as the guard voltage, pressure and RF and TW frequencies on the amount of ions that are driven through the module should be investigated, as well as how to obtain the best separation. The experiment presented here however does prove that the concept works and the settings as summarize in Table 4.4 can serve as a stepping stone for all upcoming experiments.

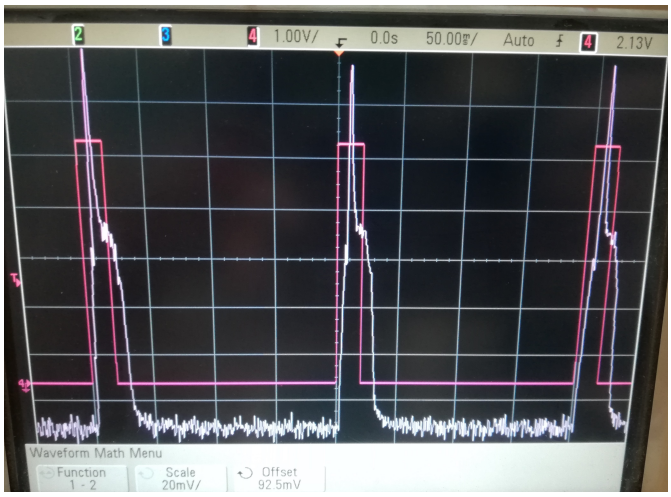

Figure 4.16: Display of oscilloscope showing the voltage pulses imposed on grid 3 (pink) and the resulting signal at the Faraday cup (white). The pink line shooting up means that the trap is switched off, allowing ions to drive through the TW-SLIM module.

Parameter	Value
Pressure	5 mbar
RF drive frequency	2.115 MHz
RF V_{pp}	370 V
TW frequency	20 kHz
TW V_{pp}	20 V
Guard voltage	3 V
Offset voltage	17 V
Trap pulse frequency	5 Hz
Trap pulse width	20 ms

Table 4.4: Values of parameters for TW-SLIM module.

4.4 Testing RIF

Even though the optimal settings for obtaining maximal signal and ion separation through the TW-SLIM module had not been found yet, it was important to see if the ions could be transported through the rear ion funnel. A Faraday cup at the end of the RIF was used to measure the ion current. The experiment was started with the settings shown in tables 4.2, 4.3 and 4.4 for all elements in front of the RIF. The RF frequency of the ion funnel was set to 783 kHz. Ion throughput was explored at an RF V_{pp} voltage of 20 V. To the first electrode of the RIF a bias of 12 V was applied, while the last electrode and CL plate were kept at 8 V and 0 V respectively. Albeit small, a "real" signal of about 20 pA could be displayed by the oscilloscope, which is shown in Figure 4.17. Like in Figure 4.16, the trap voltage and the signal of ions arriving at the Faraday cup are displayed. A clear delay in time can be seen between the trap pulse and the ion current on the Farady cup. The peaks are broad without discrete structures and exhibit unexpected behaviour. Behind the peak, the intensity of the signal drops to its minimum and then slowly starts to increase, before it really shoots up. This suggests that ions are continually driven through the ion funnel. Reason for this behaviour has not been investigated yet, but presumably it is due to the incorrect settings of the funnel. The DC gradient in the RIF at the moment is much smaller than in the other ion funnels, what could mean that the ion separation obtained from the TW-SLIM module is partially nullified since the ions move slower and the signal is spread out. Another possibility (probably in combination with the first argument) is that the voltage of the first electrode of the funnel is wrong,

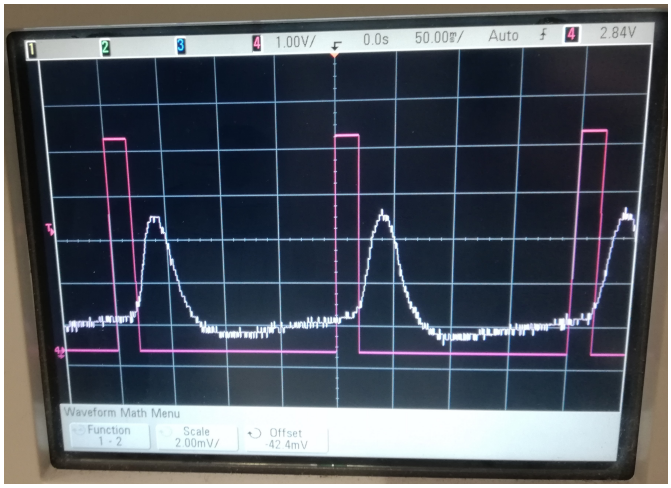

Figure 4.17: Display of oscilloscope showing the voltage pulses imposed on grid 3 (pink) and the resulting signal at the Faraday cup (white).

Parameter	**Value**
Pressure	5 mbar
RF drive frequency	783 kHz
RF V_{pp}	20 V
RIF in	12 V
RIF out	8 V
RIF CL	0 V

Table 4.5: Values of parameters for RIF.

resulting in ions being collected in front of the funnel first. They then go through it as a whole group, where some ions are travelling ahead of the group like scouts. Pressure is an additional parameter that should be explored. The signal shown in Figure 4.17 was obtained at a pressure of about 5 mbar, but no more values have systematically been investigated. In the test, the overall signal had the appearance of decreasing upon decreasing the pressure, but the influence on the width of the peaks could not be perceived immediately. At larger pressures (above 10 mbar), the signal shot up as discussed previously, indicating a possible discharge.

Despite all the deficiencies and uncertainties mentioned above, we have proven that it is possible to drive ions through the HPIF, IFT, TW-SLIM module and the RIF and obtain a measurable signal. The RIF settings summarized in Table 4.5 (together with the ones for the TW-SLIM module as given in Table 4.4) are a good starting point for future experiments. By tuning the settings then, eventually an optimal signal can be found, such that as many ions as possible can be guided through the next elements of the system (i.e. quadrupole and octupole guides, quadrupole mass filter and TOF).

Chapter 5

Outlook

The status of the IMS stage after the work of Klaas was a very good concept that consisted of machined and commercial parts. My task was to turn this into a working prototype. In the previous chapter, I showed that ions can be transported through and separated by the TW-SLIM module and that an ion current can be obtained behind the rear ion funnel. To make the extending stage ready for use at Paultje, additional experiments must be done and here a short overview of them is given.

At first, it is necessary that we get a signal at the TOF detector. Until now, it is possible to transport ions through the first two ion funnels, the TW-SLIM module and the rear funnel. The optimal settings for the TW-SLIM module and the RIF for the best signal have not been found yet. Optimization is essential to assure that as many ions as possible will make it through the first elements. To increase the signal, a different capillary with a larger internal diameter should be used as well. That way, more ions can be introduced into the system, which increases the overall ion throughput. A large throughput through the first components of the stage allows for ion losses in the next elements: the quadrupole and octupole ion guides, the quadrupole mass filter and the TOF. Ion throughput through all these components must be optimized. It is best to check the signal after each individual element to be sure that ions reach the element under investigation. It would therefore be nice if some kind of electrically insulated disk could be made that can be easily slid in between the two PCBs into the main chamber to serve as a Faraday cup. For this, an additional hole must be drilled in the main chamber, such that this disk can be placed without having to open the chamber. At the moment, the PCBs must be taken apart to install the Faraday cup, which is not practical. If instead only a small plate/disk can be placed without having to rearrange the PCB construction and opening the chamber, time is saved and the experiment is interfered less. After each new element that is introduced to the ion path, everything should be tuned to obtain the largest ion current as possible.

Then it must be investigated how the best ion separation can be obtained. Firstly with the existing PCBs, but in a later stadium with newly designed ones, in which serpentine paths and switches are used. By tuning the trap pulses and the frequency of the TW electrodes, one learns how to control the separation of the ion bunches. When making the new PCB design, it must be considered how signals at the front and back could be detected (like a Faraday cup). Thereby, a better solution for the crossing electrode paths must be found. In the PCBs used in this project, bridges of 0-Ohm resistors are used, but this is not practical in case of serpentine paths and switches due to the enormous amount of resistors needed for that. Best is to have the electric paths in different layers, such that they do not cross. For that, it is recommended to use a different software program than Sprint Layout, since this program is limited in the amount of layers.

After testing everything and optimizing the settings, the TW-SLIM stage must be connected to Paultje. Then again all elements must be tuned to one another in order to obtain the largest throughput and in the end the best ion separation.

Besides these large tasks, there are some smaller practical things that can be improved as well. For example, the BNC connector board can be mounted in a better and more stable way. Further, the wires from the chamber to the board must be better isolated to reduce the chance of them picking

up interfering signals from the lab. Lastly, all electronic devices should be collected together. At the moment they are scattered around the setup. For practical reasons it is necessary to have them all at one place. Perhaps some software could be written such that all electronic elements can be controlled from one clear program.

Hence still a lot must be done, but I am confident that the system can become operational in the near future.

Chapter 6

Conclusion

This thesis has reported the development of a TW-IMS stage to be added to an existing home-built mass spectrometer system. The system is used to investigate interactions between gas-phase biomolecules and radiation, but is unable to distinguish different conformations with identical mass-to-charge ratio in its current state. This presents a weak point, as the function of a biomolecule is usually defined by its conformation. The extending TW-IMS stage fixes this problem using the TW-SLIM technique. This versatile technique allows for compact, low-cost and easily fabricated designs that do not need high voltage conditions. Ions are released between two parallel printed circuit boards patterned with electrodes to which periodically DC potentials are applied. The travelling voltage waves created in this way cause dynamic local electric fields that, together with buffer gas molecules, determine the propagation speed of the ions through the device. The drift velocity is related to the collisional cross section and, therefore, to the molecular conformation. Hence based on differences in arrival times at the end of the boards, the different conformations can be distinguished.

The developed stage consists, besides the TW-SLIM module, of a capillary supporting system and two commercial ion funnels in front of the module. One of these funnels contains a trap, such that ions arrive at the TW-SLIM PCBs in bunches. Behind the module, a third ion funnel is situated, as well as a short quadrupole ion guide, in order to couple the stage to the existing setup. The printed circuit boards for the TW-SLIM module and their supporting frame have been designed and fabricated. Their design is a first version and consists of a linear electrode pattern to guide ions in one straight path through the vacuum chamber. Besides this main component, a number of additional elements were designed, assembled and commissioned as well, such as the capillary supporting system and the holders for the multipin feedthroughs. An existing RF quadrupole and an existing vacuum chamber for this quadrupole were adapted to the IMS system.

First experiments have been performed in order to see if ions are actually transported through the different elements of the developed stage. This was tested using a Faraday cup that converges the signal of ions hitting the cup into a measurable electric current. Throughput of ions through the individual components was measured by placing the cup behind the component under investigation. Behaviour of different parameters of the first two ion funnels, such as pressure and RF peak-to-peak voltage, have been investigated thoroughly in order to obtain optimal ion current. A maximum current of 170 pA was measured behind the IFT, which appears to be the highest value that can be obtained with the capillary currently used. Ion throughput through the TW-SLIM module and the RIF has been explored less extensively, but tests show that it is possible to transport ions through these elements as well. A signal of 100 pA was measured behind the PCBs, while a current of 20 pA could be measured behind the RIF. There is lots of room for improvement of these signals, since settings have not been optimized yet. However, already under these "bad" conditions, the response of ions to being trapped in the IFT for a certain time have been detected and displayed on an oscilloscope.

Developing a working and fully tested TW-SLIM stage was not feasible within this project. All individual elements of the stage have been developed and assembled to form one system and the working of the TW-SLIM module has been proven. However, more and thorough testing is needed before it

can actually be connected to the existing mass spectrometer system. A detailed overview of the things needed to complete this task has been given.

Once being integrated in the mass spectrometer system, the TW-SLIM module will prove to be a versatile technique to analytically separate, detect, and characterize biomolecules. By allowing the use of long ion paths with minimum losses, exceptional structural sensitivity will be perceived. The developed stage can therefore be seen as a rightful extension to the existing system.

Acknowledgements

This project could not have been finished without the help of many people and I want to thank all of them, and a few in particular.

First of all I would like to thank Marcelo for being my daily supervisor. Although being distanced by a whole ocean for more than half of the time, you were always there for me. You were always available for questions and chats, no matter what time it was at your place. I am still sorry for that time I woke you up in the night, but even then you were happy to help me out.

Furthermore I would like to thank Thomas, for being my first examiner and partially taking over the job of daily supervisor. Especially in the first few months you guided me through all the different tasks that needed to be done and you had always time for my questions.

I also want to say thank you to Caspar, for being my second examiner. Although not being in close contact with me or the research group, you were open to assess and learn about my project.

Then I want to thank Harry to share all of his lab experience with me. I have enjoyed our time together in the lab and learned a lot of skills related to experimenting.

I also want to mention Johan, who helped me a lot with the design and production of the PCBs. Even though I was not part of your research group, you spend a lot of time learning me how to make the PCB design with the software and how to solder all those small resistors on the boards. Sometimes I could imagine you would loose it when I came by your office again, but you always had time to help me out.

I want to thank Mart for helping with almost all practical aspects of the project. You learned me a lot of practical skills that I will take with me for the rest of my live. Thereby, you helped me picking the right materials and came up with good ideas to handle construction issues.

I want to thank Klaas for always being available to answer questions about the project. Thanks for sharing your knowledge about the project and your Autodesk Inventor files, this made it much easier for me to get familiar with the project.

Lastly I would like to thank all members of the QISD group that I have not mentioned yet, for their help and time spent in the lab: Subam, Lena, Tim, Wouter, Pieter, Bas, Nadav, Yining, Xin, Wen and Ronnie. Despite the special circumstances under which this project was realized and although we did not see each other that much in person, I enjoyed our time together in the lab and lunch breaks.

Bibliography

[1] F. Bray, J. Ferlay, I. Soerjomataram, R. L. Siegel, L. A. Torre, and A. Jemal, "Global cancer statistics 2018: GLOBOCAN estimates of incidence and mortality worldwide for 36 cancers in 185 countries," *CA: A Cancer Journal for Clinicians*, vol. 68, no. 6, pp. 394–424, 2018.

[2] K. K. Wong, S. Chang, S. R. Weiler, S. Ganesan, J. Chaudhuri, C. Zhu, S. E. Artandi, K. L. Rudolph, G. J. Gottlieb, L. Chin, F. W. Alt, and R. A. DePinho, "Telomere dysfunction impairs DNA repair and enhances sensitivity to ionizing radiation," *Nature Genetics*, vol. 26, no. 1, pp. 85–88, 2000.

[3] M. Ruden and N. Puri, "Novel anticancer therapeutics targeting telomerase," *Cancer Treatment Reviews*, vol. 39, no. 5, pp. 444–456, 2013.

[4] W. Li, E. Mjekiqi, W. Douma, X. Wang, O. Kavatsyuk, R. Hoekstra, J. C. Poully, and T. Schlathölter, "Hole Migration in Telomere-Based Oligonucleotide Anions and G-Quadruplexes," *Chemistry - A European Journal*, vol. 25, no. 70, pp. 16114–16119, 2019.

[5] "Schlathölter group: Gas phase biomolecules and energetic interactions." `https://www.rug.nl/research/zernike/quantum-interactions-and-structural-dynamics/schlatholter-group/`, 2017. Accessed: 16-02-2021.

[6] D. Egorov, *Photoionization and excitation processes in proteins and peptides.* PhD thesis, 2018.

[7] D. E. Clemmer and M. F. Jarrold, "Ion mobility measurements and their applications to clusters and biomolecules," *Journal of Mass Spectrometry*, vol. 32, no. 6, pp. 577–592, 1997.

[8] R. Cumeras, E. Figueras, C. E. Davis, J. I. Baumbach, and I. Gràcia, "Review on Ion Mobility Spectrometry. Part 1: Current instrumentation," *Analyst*, vol. 140, no. 5, pp. 1376–1390, 2015.

[9] P. E. Toschek, "Wolfgang Paul," *Physics Today*, vol. 47, no. 7, pp. 76–77, 1994.

[10] O. Gonzalez-Magaña, *Ionization-induced fragmentation dynamics of isolated complex biomolecules.* PhD thesis, 2013.

[11] S. Bari, *The influence of peptide structure on fragmentation pathways.* PhD thesis, 2010.

[12] J. B. Fenn, M. Mann, C. K. Meng, S. F. Wong, and C. M. Whitehouse, "Electrospray ionization for mass spectrometry of large biomolecules," *Science*, vol. 246, no. 4926, pp. 64–71, 1989.

[13] L. Konermann, E. Ahadi, A. D. Rodriguez, and S. Vahidi, "Unraveling the mechanism of electrospray ionization," *Analytical Chemistry*, vol. 85, no. 1, pp. 2–9, 2013.

[14] N. Basson, *Free volume of electrospun organic-inorganic copolymers.* PhD thesis, University of Stellenbosch, 2014.

[15] Q. Yu, Z. Diao, K. Ni, X. Qian, F. Tang, and X. Wang, "Design and study of an atmospheric pressure ion funnel by computer simulations," *Rapid Communications in Mass Spectrometry*, vol. 29, no. 11, pp. 1055–1061, 2015.

[16] R. T. Kelly, A. V. Tolmachev, J. S. Page, K. Tang, and R. D. Smith, "The ion funnel REV," *NIH Public Access*, vol. 29, no. 2, pp. 294–312, 2011.

[17] S. Guan and A. G. Marshall, "Stacked-ring electrostatic ion guide," *Journal of the American Society for Mass Spectrometry*, vol. 7, no. 1, pp. 101–106, 1996.

[18] K. Blaum, "High-accuracy mass spectrometry with stored ions," *Physics Reports*, vol. 425, no. 1, pp. 1–78, 2006.

[19] K. Bijlsma, "The development of a travelling wave ion mobility spectrometry stage for a tandem mass spectrometer." 2019.

[20] M. M. Wolff and W. E. Stephens, "A pulsed mass spectrometer with time dispersion," *Review of Scientific Instruments*, vol. 24, no. 8, pp. 616–617, 1953.

[21] E. V. Moskovets, "Mass-reflectron as an ion energy analyzer," *Applied Physics B Photophysics and Laser Chemistry*, vol. 54, no. 6, pp. 556–561, 1992.

[22] K. Fouque, *Differentiation of Peptide Topoisomers Using Ion Mobility - Mass Spectrometry and Tandem Spectrometry*. PhD thesis, Florida International University, 2016.

[23] H. E. Revercomb and E. A. Mason, "Theory of Plasma Chromatography/Gaseous Electrophoresis. A Review," *Analytical Chemistry*, vol. 47, no. 7, pp. 970–983, 1975.

[24] "Mean free path and collision frequency." `https://www.tec-science.com/thermodynamics/kinetic-theory-of-gases/mean-free-path-collision-frequency/`, 2019. Accessed: 16-11-2020.

[25] M. T. Bowers, "Ion mobility spectrometry: A personal view of its development at UCSB," *International Journal of Mass Spectrometry*, vol. 370, pp. 75–95, 2014.

[26] K. Giles, S. D. Pringle, K. R. Worthington, D. Little, J. L. Wildgoose, and R. H. Bateman, "Applications of a travelling wave-based radio-frequency-only stacked ring ion guide," *Rapid Communications in Mass Spectrometry*, vol. 18, no. 20, pp. 2401–2414, 2004.

[27] A. A. Shvartsburg and R. D. Smith, "Fundamentals of traveling wave ion mobility spectrometry," *Analytical Chemistry*, vol. 80, no. 24, pp. 9689–9699, 2008.

[28] A. V. Tolmachev, I. K. Webb, Y. M. Ibrahim, S. V. Garimella, X. Zhang, G. A. Anderson, and R. D. Smith, "Characterization of Ion Dynamics in Structures for Lossless Ion Manipulations," *Analytical Chemistry*, vol. 86, no. 18, pp. 9162–9168, 2014.

[29] S. V. Garimella, Y. M. Ibrahim, I. K. Webb, A. V. Tolmachev, X. Zhang, S. A. Prost, G. A. Anderson, and R. D. Smith, "Simulation of electric potentials and ion motion in planar electrode structures for lossless ion manipulations (SLIM)," *Journal of the American Society for Mass Spectrometry*, vol. 25, no. 11, pp. 1890–1896, 2014.

[30] X. Zhang, S. V. Garimella, S. A. Prost, I. K. Webb, T. C. Chen, K. Tang, A. V. Tolmachev, R. V. Norheim, E. S. Baker, G. A. Anderson, Y. M. Ibrahim, and R. D. Smith, "Ion Trapping, Storage, and Ejection in Structures for Lossless Ion Manipulations," *Analytical Chemistry*, vol. 87, no. 12, pp. 6010–6016, 2015.

[31] A. M. Hamid, Y. M. Ibrahim, S. V. Garimella, I. K. Webb, L. Deng, T. C. Chen, G. A. Anderson, S. A. Prost, R. V. Norheim, A. V. Tolmachev, and R. D. Smith, "Characterization of Traveling Wave Ion Mobility Separations in Structures for Lossless Ion Manipulations," *Analytical Chemistry*, vol. 87, no. 22, pp. 11301–11308, 2015.

[32] A. M. Hamid, S. V. Garimella, Y. M. Ibrahim, L. Deng, X. Zheng, I. K. Webb, G. A. Anderson, S. A. Prost, R. V. Norheim, A. V. Tolmachev, E. S. Baker, and R. D. Smith, "Achieving High Resolution Ion Mobility Separations Using Traveling Waves in Compact Multiturn Structures for Lossless Ion Manipulations," *Analytical Chemistry*, vol. 88, no. 18, pp. 8949–8956, 2016.

[33] S. V. Garimella, A. M. Hamid, L. Deng, Y. M. Ibrahim, I. K. Webb, E. S. Baker, S. A. Prost, R. V. Norheim, G. A. Anderson, and R. D. Smith, "Squeezing of ion populations and peaks in traveling wave ion mobility separations and structures for lossless ion manipulations using compression ratio ion mobility programming," *Analytical Chemistry*, vol. 88, no. 23, pp. 11877–11885, 2016.

[34] Y. M. Ibrahim, A. M. Hamid, L. Deng, S. V. Garimella, I. K. Webb, E. S. Baker, and R. D. Smith, "New frontiers for mass spectrometry based upon structures for lossless ion manipulations," *Analyst*, vol. 142, no. 7, pp. 1010–1021, 2017.

[35] L. Deng, I. K. Webb, S. V. Garimella, A. M. Hamid, X. Zheng, R. V. Norheim, S. A. Prost, G. A. Anderson, J. A. Sandoval, E. S. Baker, Y. M. Ibrahim, and R. D. Smith, "Serpentine Ultralong Path with Extended Routing (SUPER) High Resolution Traveling Wave Ion Mobility-MS using Structures for Lossless Ion Manipulations," *Analytical Chemistry*, vol. 89, no. 8, pp. 4628–4634, 2017.

[36] A. L. Hollerbach, A. Li, A. Prabhakaran, G. Nagy, C. P. Harrilal, C. R. Conant, R. V. Norheim, C. E. Schimelfenig, G. A. Anderson, S. V. Garimella, R. D. Smith, and Y. M. Ibrahim, "Ultra-High-Resolution Ion Mobility Separations over Extended Path Lengths and Mobility Ranges Achieved using a Multilevel Structures for Lossless Ion Manipulations Module," *Analytical Chemistry*, vol. 92, no. 11, pp. 7972–7979, 2020.

[37] Y. M. Ibrahim, A. M. Hamid, J. T. Cox, S. V. Garimella, and R. D. Smith, "Ion Elevators and Escalators in Multilevel Structures for Lossless Ion Manipulations," *Analytical Chemistry*, vol. 89, no. 3, pp. 1972–1977, 2017.

[38] R. Veenstra. Private communication.

[39] Y. Ibrahim, M. E. Belov, A. V. Tolmachev, D. C. Prior, and R. D. Smith, "Ion funnel trap interface for orthogonal time-of-flight mass spectrometry," *Analytical Chemistry*, vol. 79, no. 20, pp. 7845–7852, 2007.

[40] "Product data of PTFE." `https://www.spacematdb.com/spacemat/datasearch.php?name=PTFE`. Accessed: 29-01-2021.

[41] L. Deng, Y. M. Ibrahim, A. M. Hamid, S. V. Garimella, I. K. Webb, X. Zheng, S. A. Prost, J. A. Sandoval, R. V. Norheim, G. A. Anderson, A. V. Tolmachev, E. S. Baker, and R. D. Smith, "Ultra-High Resolution Ion Mobility Separations Utilizing Traveling Waves in a 13 m Serpentine Path Length Structures for Lossless Ion Manipulations Module," *Analytical Chemistry*, vol. 88, no. 18, pp. 8957–8964, 2016.

[42] "Pcb & assembly services – pcb proto." `https://www.eurocircuits.com/pcb-assembly-proto/`. Accessed: 25-11-2020.

[43] G. Anderson. Private communication.

[44] A. M. Hamid, A. Prabhakaran, S. V. Garimella, Y. M. Ibrahim, and R. D. Smith, "Characterization of applied fields for ion mobility separations in traveling wave based structures for lossless ion manipulations (SLIM)," *International Journal of Mass Spectrometry*, vol. 430, pp. 8–13, 2018.

[45] "Sprint-layout 6.0." `https://sprint-layout.software.informer.com/6.0/`. Accessed: 26-01-2021.

[46] J. Holstein. Private communication.

[47] "JLCPCB website." https://jlcpcb.com/. Accessed: 29-01-2021.

[48] "Vishay 0-Ohm, 0402 (1005m) thick film SMD resistor." https://nl.rs-online.com/web/p/surface-mount-fixed-resistors/3932326/?relevancy-data=7365617263685F636173636164655F6F726465723D31267365617263685F696E746572666163655F6E616D653D493138&searchHistory=%7B%22enabled%22%3Atrue%7D. Accessed: 29-01-2021.

[49] "Inventor by Autodesk." https://www.autodesk.co.uk/products/inventor/overview?plc=INVPROSA&term=1-YEAR&support=ADVANCED&quantity=1. Accessed: 05-11-2020.